Contents

1 Third Sound **4**
- 1.1 Introduction . . . 4
- 1.2 Third sound speed . . . 5
- 1.3 Third sound attenuation . . . 6
- 1.4 Film thickness . . . 8
  - 1.4.1 The vapour pressure p_v . . . 8
  - 1.4.2 The number of ^{4}He atoms in the cell N . . . 8
  - 1.4.3 The third sound speed c_3 . . . 9

2 Phonon modes in thin films recalculated **10**
- 2.1 Introduction . . . 10
- 2.2 A new phonon distribution function . . . 10
  - 2.2.1 Crystal dimensions . . . 10
  - 2.2.2 The density of states over ω . . . 11
  - 2.2.3 Angular dependence of phonon density . . . 12
  - 2.2.4 The density of states over ω recalculated as a check . . . 13
  - 2.2.5 Taking into account discreteness of k_y . . . 14
  - 2.2.6 The density of states over θ . . . 15
- 2.3 Monte Carlo simulations . . . 17
- 2.4 Kapitza resistance . . . 20
  - 2.4.1 Heat flux . . . 20
  - 2.4.2 Kapitza resistance . . . 21
- 2.5 Discussion . . . 22
  - 2.5.1 Experimental support . . . 22
  - 2.5.2 Suggestions for improvement . . . 23

3 Experimental set-up **24**
- 3.1 Cryogenics . . . 24
- 3.2 The cell . . . 25
- 3.3 The bar geometry . . . 26
- 3.4 Electrolytic polishing of copper . . . 27
- 3.5 Excitation of third sound . . . 30
- 3.6 Detection of third sound . . . 31
- 3.7 Gas handling system . . . 31

4 Experimental results **33**
4.1 Third sound signals . . . 33
4.2 Third sound speed . . . 36
4.2.1 Comparison of $c_{3,gl}$ and $c_{3,Cu}$ . . . 36
4.2.2 Calculation of δ_{gl} and δ_{Cu} . . . 37
4.2.3 $c_{3,Cu}$ versus δ_{Cu} . . . 38
4.3 Third sound attenuation . . . 39
4.3.1 Calculation of the attenuation coefficient α . . . 39
4.3.2 Attenuation on the glass bar . . . 39
4.3.3 Attenuation on the copper bar . . . 40
4.4 Discussion and conclusions . . . 41
4.4.1 Third sound on copper . . . 41
4.4.2 Comparison with Brisson's experiments . . . 41
4.4.3 Attenuation coefficient on copper . . . 41
4.4.4 Problem: Pressure determination . . . 42
4.4.5 Problem: Film thickness determination error . . . 42

A Drawings **43**

B Symbols **49**

List of Figures

1.1 Third sound speed c_3 in ^{4}He on glass as a function of film thickness δ 6
1.2 Attenuation coefficient α on glass as a function of film thickness δ 7
1.3 Attenuation coefficient α on copper as a function of film thickness δ 7

2.1 Phonon $\vec{k}$-vectors with $\omega_{\vec{k}} < 5$ 12
2.2 Distribution function over ω for $\omega < 0.1 \cdot 10^{15}\,\mathrm{s}^{-1}$ 18
2.3 Distribution function over ω for $\omega < 10^{12}\mathrm{s}^{-1}$ 18
2.4 Distribution function over ω for $\omega < 10^{9}\,\mathrm{s}^{-1}$ 19
2.5 Distribution function over θ for $\omega < 10^{12}\mathrm{s}^{-1}$ 19
2.6 Kapitza resistance between gold heater and glass substrate as a function of T . . . 22

3.1 Pumped ^{4}He cryostat 24
3.2 Experimental cell 25
3.3 Twin bars setup 26
3.4 Setup for electropolishing the copper bar 27
3.5 Electrical circuit for electropolishing 28
3.6 Typical electropolishing I, V-diagram 28
3.7 Heater on copper 30
3.8 Excitation electronics 30
3.9 Tunnel diode and filtering electronics 31
3.10 Detection system 31
3.11 Gas handling system 32

4.1 Third sound signal on glass. $n_{\mathrm{in}} = 16.83$ mmol 34
4.2 Third sound signal on glass. $n_{\mathrm{in}} = 35.9$ mmol 35
4.3 Third sound signal on copper. $n_{\mathrm{in}} = 35.9$ mmol 35
4.4 Third sound speed c_3 on copper and on glass as a function of the amount of ^{4}He in the cell 36
4.5 Third sound speed $c_{3,Cu}$ on copper as a function of ^{4}He film thickness δ_{Cu} 38
4.6 Third sound attenuation α on glass as a function of ^{4}He film thickness δ 39
4.7 Third sound attenuation α on copper as a function of ^{4}He film thickness δ_{Cu} . . . 40
4.8 Brisson's heater 41

A.1 Bottom plate in experimental cell 43
A.2 Left frame piece 44
A.3 Right frame piece 45
A.4 Copper resonator bar 46
A.5 Glass resonator bar 47
A.6 Mounting platform 48

Chapter 1

Third Sound

1.1 Introduction

Liquid ^{4}He becomes a superfluid, i.e., it can flow without friction, below the λ-temperature (2.18 K). Superfluid ^{4}He can be described by the two-fluids model[1]. This model states that the liquid consists of two parts:

- A normal part that is viscous and carries entropy.
- A superfluid part that is not viscous and does not carry entropy.

In a superfluid ^{4}He film, a surface wave called *third sound* can be excited. Only the superfluid part takes part in the surface wave, because the normal part is stuck to the wall as long as the viscous penetration depth is smaller than the film thickness. Third sound consists of both temperature and film thickness oscillations and can be excited by either a heat pulse or a strong electric field.

Third sound has been studied extensively, mostly on a glass substrate[7]. Subjects of study have been the propagation speed and the damping coefficient, as a function of film thickness and temperature.

To extend these experiments to ^{3}He, the film has to be cooled below 0.93 mK, the ^{3}He superfluid transition temperature. Because it is hard to cool glass to these temperatures, a copper substrate has to be used. Experiments with third sound on a copper substrate, using ^{4}He, have been described previously [14]. In these experiments a copper cylinder was used which enabled resonant measuments; in previous experiments of the same group a flat glass surface was used so that only time-of-flight measurements could be performed.

The present work was undertaken to link previous experiments with a copper cylinder to those with glass. For this, an experimental cell that contains both a glass and a copper cylinder was built in order to measure properties, especially third sound speed and attenuation, of third sound on both substrates under the same circumstances.

The experiments described in this report involve the use of a thin gold heater to excite the third sound. Theoretical work on phonon modes and Kapitza resistances at low temperatures and with thin materials was performed as well (Chapter 2).

All symbols used in this paper are given in Appendix B.

1.2 Third sound speed

From the film equations of the two-fluids model the following equation for the third sound speed can be derived[1]:

$$c_3^2 = \left(\frac{\rho_s}{\rho}\right)_f f(\delta)\,\delta \tag{1.1}$$

with

$$\left(\frac{\rho_s}{\rho}\right)_f = \left(\frac{\rho_s}{\rho}\right)\frac{\delta - D(T)}{\delta} \tag{1.2}$$

$$f(\delta) = \frac{\partial\Omega}{\partial\delta} \tag{1.3}$$

$$\Omega = -\frac{\gamma}{\delta^3\left(1+\frac{\delta}{\beta}\right)} \tag{1.4}$$

Where

$$\begin{aligned}
c_3 &= \text{Third sound speed } (\mathrm{m\,s^{-1}}) \\
D(T) &= \text{Non-superfluid layer (see below)} \\
T &= \text{Temperature (K)} \\
\left(\frac{\rho_s}{\rho}\right) &= \text{Superfluid fraction in bulk } {}^4\mathrm{He} \\
\left(\frac{\rho_s}{\rho}\right)_f &= \text{Average superfluid fraction of the film} \\
f(\delta) &= \text{Van der Waals attractive force } (\mathrm{m\,s^{-2}}) \\
\delta &= {}^4\text{He film thickness (m)} \\
\Omega &= \text{Van der Waals potential } (\mathrm{m^2 s^{-2}}) \\
\gamma &= \text{Van der Waals constant } (\gamma = 2.6\cdot 10^{-24}\,\mathrm{m^5 s^{-2}} \text{ for glass}) \\
\beta &= \text{Retardation constant } (\beta = 15\,\mathrm{nm} \text{ for glass})
\end{aligned}$$

$D(T)$ is the “dead layer”, the part, of typically a few atomic layers, of the film that is not superfluid and does not take part in third sound. Below 0.6 K, $D(T) = 1.47\,\mathrm{a.l.}$ (1 a.l. = one atomic layer or 0.36 nm.) Above 0.6 K,

$$D(T) = A + B\cdot T\left(\frac{\rho}{\rho_s}\right) \tag{1.5}$$

with $A = 0.5\,\mathrm{a.l.}$ and $B = 1.13\,\mathrm{a.l.K^{-1}}$[7]. In Figure 1.1, the third sound speed on glass is plotted against film thickness for various temperatures using Equation 1.1. For $\left(\frac{\rho_s}{\rho}\right)$ data is taken from Wilks[18, p. 62].

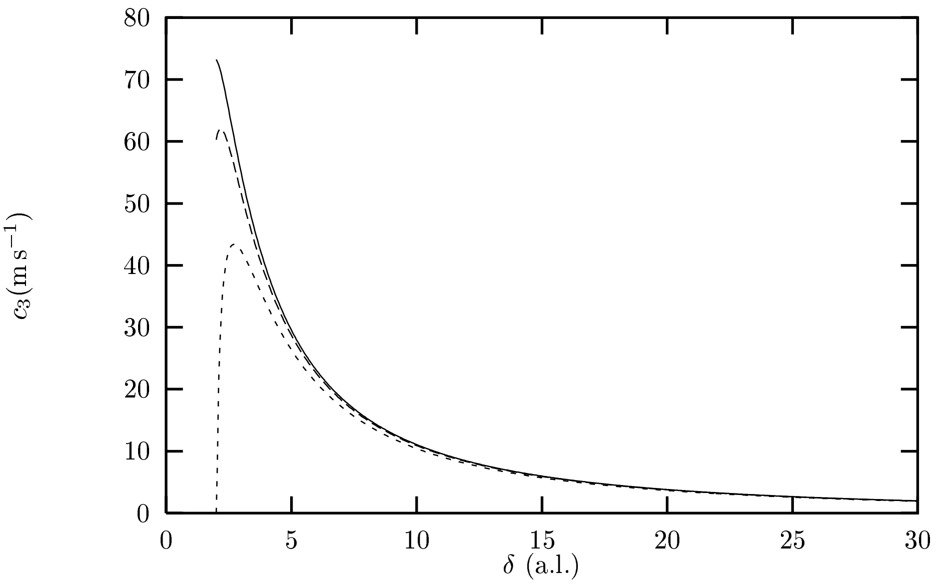

Figure 1.1: Third sound speed c_3 in ^{4}He on glass as a function of film thickness δ. Solid line: $T = 0.5\,\mathrm{K}$; Long dashes: $T = 1.0\,\mathrm{K}$; Short dashes: $T = 1.3\,\mathrm{K}$

1.3 Third sound attenuation

The third sound attenuation coefficient α is defined by the following equation:

$$A(x) = A(0) \cdot e^{-\alpha x} \tag{1.6}$$

with $A(x)$ the amplitude of the third sound wave after running a distance x. The unit of α is m^{-1}. Brouwer[4] and Draisma[7] give an elaborate treatment of the theory of third sound, including attenuation, for temperatures above $\approx 1\,\mathrm{K}$. Distinction is made between finite geometries (with two substrate plates and ^{4}He films opposite to each other, at a distance of 2 to 50 μm) and the infinite geometry (with no opposite plate), as used in the experiments described in Chapter 4. For thin films, the dominant damping mechanisms are the thermal waves induced in the ^{4}He vapour and in the substrate. For thicker films, the acoustic wave in the vapour becomes the dominant damping mechanism.

The results from this theory, for 4.17 kHz third sound and the infinite geometry, are presented in Figure 1.2 for a glass substrate and in Figure 1.3 for a copper substrate. These calculations were performed using a program written by Brouwer[5]. The minimums in these plots indicate the transition from the thin-film to the thick-film region, where the dominant damping mechanism shifts from thermal to acoustic waves.

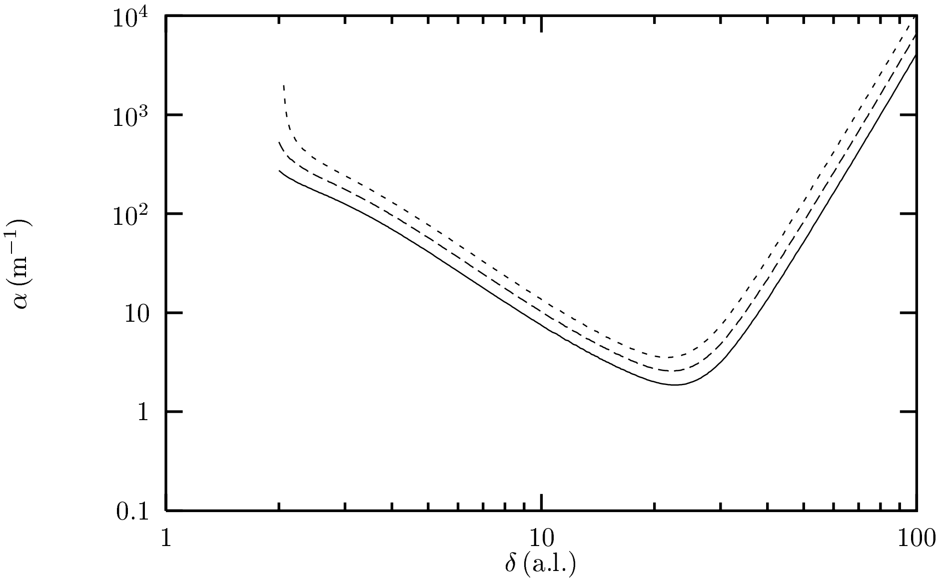

Figure 1.2: Attenuation coefficient α on glass as a function of film thickness δ, according to Brouwer[4, 5]. $\nu = 4.17\,\mathrm{kHz}$, infinite geometry. Solid line: $T = 1.10\,\mathrm{K}$; Long dashes: $T = 1.21\,\mathrm{K}$; Short dashes: $T = 1.30\,\mathrm{K}$.

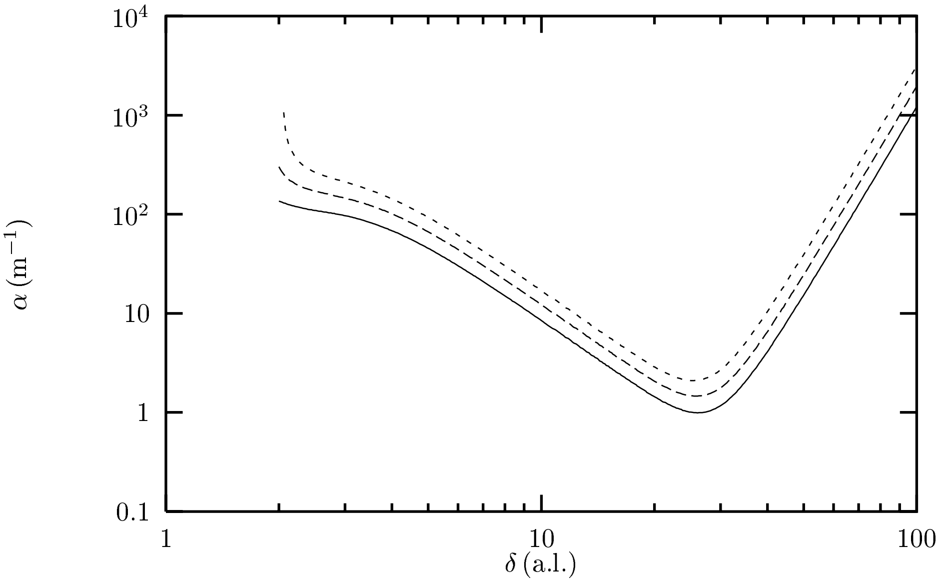

Figure 1.3: Attenuation coefficient α on copper as a function of film thickness δ, according to Brouwer[4, 5]. $\nu = 4.17\,\mathrm{kHz}$, infinite geometry. Solid line: $T = 1.10\,\mathrm{K}$; Long dashes: $T = 1.21\,\mathrm{K}$; Short dashes: $T = 1.30\,\mathrm{K}$.

1.4 Film thickness

There are several ways to determine the helium film thickness on the walls of a container. The determination can be performed with the use of one of the following parameters:

- The vapour pressure p_v
- The number of ^{4}He atoms in the cell N
- The third sound speed c_3.

1.4.1 The vapour pressure p_v

At a distance x from a surface, the helium pressure p can be expressed as [7, p. 65]

$$p = p_v \, e^{-\frac{m\Omega(x)}{k_B T}} \tag{1.7}$$

Here p_v is the vapour pressure in the container, Ω is the Van der Waals potential, k_B is Boltzmann's constant and m is the mass of a ^{4}He atom. The helium film–vapour interface will appear at a distance δ (the film thickness) from the surface, where pressure p equals the saturated vapour pressure p_{sv}:

$$p_{sv} = p_v \, e^{-\frac{m\Omega(\delta)}{k_B T}} \tag{1.8}$$

Rewriting this formula using Equation 1.4 gives

$$\delta^3 = \delta_0^3 - \frac{1}{\beta}\delta^4 \tag{1.9}$$

with

$$\delta_0^{-3} = \frac{k_B T}{\gamma m} \ln \frac{p_{sv}}{p_v} \tag{1.10}$$

The film thickness δ can now be calculated recursively using these formulas if T and p_v are measured (because p_{sv} depends on T only).

1.4.2 The number of ^{4}He atoms in the cell N

The film thickness δ can also be calculated if the total number of ^{4}He atoms in the film N_{film} is known:

$$N_{\text{film}} = S \cdot n \cdot \delta \tag{1.11}$$

with S the inner area of the container and n the bulk ^{4}He density. However, the ^{4}He density in the first one or two layers will be higher than the bulk density because of the strong Van der Waals interaction. To take this into account Equation 1.11 is rewritten as

$$N_{\text{film}} - N_0 = S \cdot n \cdot \delta \tag{1.12}$$

Here N_0 is the extra number of ^{4}He atoms in the first one or two layers. To calculate N_{film} from the total number of ^{4}He atoms in the cell N the number of ^{4}He atoms in the vapour is required:

$$N_{\text{vapour}} = \frac{p_v V}{k_B T} \tag{1.13}$$

Using Equation 1.8 yields:

$$N_{\text{vapour}} = \frac{p_{sv}(T)V}{k_B T}\, e^{\frac{m\Omega(\delta)}{k_B T}} \tag{1.14}$$

Since

$$N = N_{\text{film}} + N_{\text{vapour}}$$

the following result is obtained:

$$N = N_0 + S \cdot n \cdot \delta + \frac{p_{sv}(T)V}{k_B T}\, e^{\frac{m\Omega(\delta)}{k_B T}} \tag{1.15}$$

Rewriting the last equation gives

$$\delta = \frac{N}{Sn} - \frac{N_0}{Sn} - \frac{p_{sv}(T)V}{k_B T}\, e^{\frac{m\Omega(\delta)}{k_B T}} \tag{1.16}$$

which can be solved recursively to determine δ if N, T, S and V are known. The value $\frac{N_0}{Sn} = (0.98 \pm 0.09)$ a.l. has been determined by Draisma [7].

1.4.3 The third sound speed c_3

The film thickness can be calculated recursively using Equation 1.1 if c_3 and T are known.

Chapter 2

Phonon modes in thin films recalculated

2.1 Introduction

In third sound experiments, a thin gold film (thickness $\leq$ 100 nm) is often used as a heater to excite the third sound wave [7]. An effect of the thinness of this film on the heat transfer from the heater to the substrate was suspected because, at low temperature T, the typical phonon wavelength λ, calculated with

$$E = k_B T = \hbar\omega = \hbar c \left|\vec{k}\right| = \hbar c \cdot \frac{2\pi}{\lambda}$$

becomes 160 nm when using $T = 1$ K and sound velocity $c = 3390\,\mathrm{m\,s^{-1}}$. This value is of the same order of magnitude as the heater thickness.

Therefore an alternative for the standard (Debye) phonon distribution function was developed and tested by Monte Carlo simulation. Furthermore the Kapitza resistance between the film and another material was recalculated using the new phonon distribution function.

2.2 A new phonon distribution function

2.2.1 Crystal dimensions

All calculations will be performed assuming the film is a solid of dimensions $V = L_x \times L_y \times L_z$ with a cubic lattice with lattice parameter a. There are $N = N_x \times N_y \times N_z$ atoms in the crystal. The speed of sound in the solid is c. Only longitudinal phonons will be take into account. This treatment can easily be generalized to other phonon polarizations.

The phonon (reciprocal lattice) vectors take the form $\vec{k} = (k_x, k_y, k_z)$ with

$$k_i = \frac{2\pi}{L_i} \cdot n_i \tag{2.1}$$

Here the k_i are limited to $-\frac{\pi}{a} \cdots \frac{\pi}{a}$ and thus the (integer) n_i to the values $-\frac{N_i}{2} \cdots \frac{N_i}{2}$.

Assuming $L_z \ll L_y \ll L_x$ it follows that the values of k_x and k_y are much more closely spaced than the values of k_z. Therefore k_x and k_y will be assumed to be continuous, while k_z will be considered discrete.

2.2.2 The density of states over ω

The density of states over ω (i.e. the number of phonon states with circular frequency between ω and $\omega + d\omega$) is described [6, p. 216] under the approximation of a continuous distribution of $\vec{k}$-vectors by

$$g(\omega)\, d\omega = \frac{V\omega^2}{2\pi^2 c^3} \tag{2.2}$$

In the following treatment discrete values will be used for k_z. First the density of states for a fixed value of k_z is calculated. Then this result is summed for all possible values of k_z.

Because the circular frequency of a phonon mode $\vec{k}$ equals

$$\omega_{\vec{k}}{}^2 = \left(c\left|\vec{k}\right|\right)^2 = c^2\left(k_x^2 + k_y^2 + k_z{}^2\right) \tag{2.3}$$

it follows that

$$k_x^2 + k_y^2 = \frac{\omega_{\vec{k}}^2}{c^2} - k_z{}^2$$

The number of $\vec{k}$-values with $\omega_{\vec{k}} < \omega$ for a fixed value of k_z equals

$$N_{\omega_{\vec{k}}<\omega} = \pi\left(\frac{\omega^2}{c^2} - k_z^2\right)\frac{L_x L_y}{(2\pi)^2}$$

with $\pi\left(\frac{\omega^2}{c^2} - k_z^2\right)$ the "area" of the circle in $\vec{k}$-space and $\frac{L_x L_y}{(2\pi)^2}$ the surface density of states on that area. As an example, in figure 2.1, the sphere depicts

$$k_x{}^2 + k_y{}^2 + k_z{}^2 = \frac{\omega}{c} = 5$$

The planes represent constant values of

$$k_z = \frac{2\pi}{L_z}\cdot n_i = 2\cdot n_i$$

The dark circles thus represent $\vec{k}$-vectors with $\vec{k}^2 < 5$. In this case, $k_z \in \{-4, -2, 0, 2, 4\}$ are the possible values of k_z with $\omega_{\vec{k}} < \frac{\sqrt{5}}{c}$.

The number of modes with circular frequency between ω and $\omega + d\omega$ at the fixed value of k_z now equals

$$\begin{aligned} g_{k_z}(\omega)\, d\omega &= \frac{\partial}{\partial\omega}\left(N_{\omega_{\vec{k}}<\omega}\right) d\omega \\ &= \frac{L_x L_y}{2\pi c^2}\omega\, d\omega \end{aligned}$$

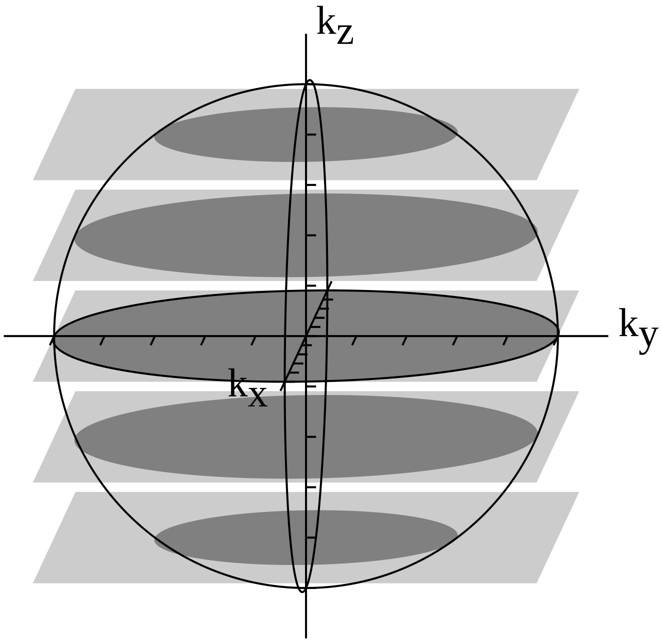

Figure 2.1: Phonon $\vec{k}$-vectors with $\omega_{\vec{k}} < 5$

For $\omega < c\frac{2\pi}{L_z}$, only the modes with $k_z = 0$ are present (eq. 2.1 and 2.3), so $g(\omega) = \frac{L_x L_y}{2\pi c^2}\omega$ for $\omega < c\frac{2\pi}{L_z}$. For $c\frac{2\pi}{L_z} \leq \omega < 2c\frac{2\pi}{L_z}$, 3 k_z-values are possible ($k_z = -1, 0, 1 \cdot \frac{2\pi}{L_z}$), etc. The total number of modes becomes

$$g(\omega)\, d\omega = \frac{L_x L_y}{2\pi c^2} \cdot \omega \cdot \left(1 + 2\left\lfloor \frac{L_z \omega}{2\pi c} \right\rfloor\right) d\omega \tag{2.4}$$

where $\lfloor x \rfloor$ means the largest integer smaller than or equal to x.

This equation is tested using Monte Carlo techniques (section 2.3). Note that for large values of ω equation 2.4 becomes equal to equation 2.2.

2.2.3 Angular dependence of phonon density

The values of $\vec{k}$ do not have a uniform angular distribution because of the discreteness of the values of k_z. Therefore the phonon density of states is not only a function of ω (depending on the absolute value of $\vec{k}$ only), but also a function of the phonon directions.

The density of states in every k_x, k_y-plane is $\frac{L_x L_y}{(2\pi)^2}$ (there is one phonon state in every area $\frac{2\pi}{L_x} \cdot \frac{2\pi}{L_y}$). The Dirac δ-function must be used because the k_x, k_y-planes lie a distance $\frac{2\pi}{L_z}$ apart. The phonon density of states as a function of $\vec{k}$ is

$$g(k_x, k_y, k_z)\, dk_x\, dk_y\, dk_z = \frac{L_x L_y}{(2\pi)^2} \cdot \sum_{n \in \mathcal{Z}} \delta\left(k_z - \frac{2\pi}{L_z} \cdot n\right) dk_x\, dk_y\, dk_z \tag{2.5}$$

with $\mathcal{Z}$ the set of all integer numbers. This function is only valid for sufficiently small values of $\vec{k}$ (see section 2.2.1).

This differential function is transformed into the new coordinates ω, θ, ϕ with

$$\begin{aligned} k_x &= \frac{\omega}{c}\sin\theta\cos\phi \\ k_y &= \frac{\omega}{c}\sin\theta\sin\phi \\ k_z &= \frac{\omega}{c}\cos\theta \end{aligned} \tag{2.6}$$

Here ω is the circular frequency, while θ and ϕ are given by the direction of the phonon. The density of states as a function of these new variables becomes

$$g(\omega,\theta,\phi)\,d\omega\,d\theta\,d\phi = g(k_x,k_y,k_z)\cdot\frac{\omega^2}{c^3}\sin\theta\,d\omega\,d\theta\,d\phi$$

where $\frac{\omega^2}{c^3}\sin\theta$ is the Jacobian of this transformation. Thus

$$\begin{aligned} g(\omega,\theta,\phi)\,d\omega\,d\theta\,d\phi &= \frac{L_xL_y}{(2\pi)^2}\cdot\sum_{n\in\mathcal{Z}}\delta\left(\frac{\omega}{c}\cos\theta-\frac{2\pi}{L_z}\cdot n\right)\cdot\frac{\omega^2}{c^3}\sin\theta\,d\omega\,d\theta\,d\phi \\ &= \frac{L_xL_yL_z}{(2\pi c)^3}\cdot\sum_{n\in\mathcal{Z}}\delta\left(\frac{L_z\omega}{2\pi c}\cos\theta-n\right)\cdot\omega^2\sin\theta\,d\omega\,d\theta\,d\phi \end{aligned} \tag{2.7}$$

Again, this is only valid for $\omega < c\frac{\pi}{a}$ (then the k_i are always smaller than $\frac{\pi}{a}$).

If the discreteness of the values of k_z is neglected, the density of states as a function of $\vec{k}$ becomes

$$g_{\text{class}}(k_x,k_y,k_y)\,dk_x\,dk_y\,dk_z = \frac{L_xL_yL_z}{(2\pi)^3} \tag{2.8}$$

Now the density of states as a function of ω, θ, ϕ becomes

$$g_{\text{class}}(\omega,\theta,\phi)\,d\omega\,d\theta\,d\phi = \frac{L_xL_yL_z}{(2\pi)^3}\cdot\frac{\omega^2}{c^3}\,\sin\theta\;d\omega\,d\theta\,d\phi \tag{2.9}$$

2.2.4 The density of states over ω recalculated as a check

The density of states over ω is recalculated to check equation 2.7 by integrating it with respect to θ and ϕ.

$$\begin{aligned} g(\omega)\,d\omega &= \int_0^\pi d\theta\int_0^{2\pi}d\phi\,g(\omega,\theta,\phi)\,d\omega \\ &= \int_0^\pi d\theta\int_0^{2\pi}d\phi\,\frac{L_xL_yL_z}{(2\pi c)^3}\cdot\sum_{n\in\mathcal{Z}}\delta\left(\frac{L_z\omega}{2\pi c}\cos\theta-n\right)\cdot\omega^2\sin\theta\,d\omega \\ &= \frac{L_xL_yL_z}{(2\pi c)^3}\cdot 2\pi\cdot\omega^2\sum_{n\in\mathcal{Z}}\int_{-1}^{+1}d\cos\theta\,\frac{2\pi c}{L_z\omega}\delta\left(\cos\theta-\frac{2\pi c}{L_z\omega}\cdot n\right)d\omega \\ &= \frac{L_xL_y}{2\pi c^2}\cdot\omega\sum_{n\in\mathcal{Z}}\int_{-1}^{+1}d\cos\theta\,\delta\left(\cos\theta-\frac{2\pi c}{L_z\omega}\cdot n\right)d\omega \end{aligned}$$

The integral in this expression differs from zero only when

$$\frac{2\pi c}{L_z \omega} \cdot n \in [-1, 1]$$

or

$$n \in \left[-\frac{L_z \omega}{2\pi c}, \frac{L_z \omega}{2\pi c} \right]$$

Its value then becomes 1. The sum becomes $1 + 2 \left\lfloor \frac{L_z \omega}{2\pi c} \right\rfloor$, so that

$$g(\omega)\, d\omega = \frac{L_x L_y}{2\pi c^2} \cdot \omega \cdot \left(1 + 2 \left\lfloor \frac{L_z \omega}{2\pi c} \right\rfloor \right)\, d\omega$$

which equals equation 2.4.

2.2.5 Taking into account discreteness of k_y

If it is assumed that $L_z \ll L_y \ll L_x$ the discreteness of k_y can be taken into account, just like the discreteness of k_z in the previous sections. The phonon density of states as a function of $\vec{k}$ now becomes

$$g(k_x, k_y, k_z)\, dk_x\, dk_y\, dk_z = \frac{L_x}{2\pi} \sum_{n_y \in \mathcal{Z}} \sum_{n_z \in \mathcal{Z}} \delta\left(k_y - \frac{2\pi}{L_y} n_y \right) \delta\left(k_z - \frac{2\pi}{L_z} n_z \right)\, dk_x\, dk_y\, dk_z$$

and as a function of ω, θ, ϕ

$$\begin{aligned} & g(\omega, \theta, \phi)\, d\omega\, d\theta\, d\phi = \\ & \quad \frac{L_x L_y L_z}{(2\pi c)^3} \sum_{n_y \in \mathcal{Z}} \sum_{n_z \in \mathcal{Z}} \delta\left(\frac{L_y \omega}{2\pi c} \sin\theta \sin\phi - n_y \right) \delta\left(\frac{L_z \omega}{2\pi c} \cos\theta - n_z \right) \cdot \\ & \quad \omega^2 \sin\theta\, d\omega\, d\theta\, d\phi \end{aligned}$$

The distribution function over ω will be calculated in the region where $\omega < 2\pi c / L_z$, so $k_z = 0$.

$$\begin{aligned} & g(\omega)\, d\omega = \\ & \quad \int_0^{\pi} d\theta \int_0^{2\pi} d\phi\, \frac{L_x L_y L_z}{(2\pi c)^3} \sum_{n_y \in \mathcal{Z}} \sum_{n_z \in \mathcal{Z}} \delta\left(\frac{L_y \omega}{2\pi c} \sin\theta \sin\phi - n_y \right) \delta\left(\frac{L_z \omega}{2\pi c} \cos\theta - n_z \right) \cdot \\ & \quad \omega^2 \sin\theta\, d\omega \\ & = \frac{L_x L_y L_z}{(2\pi c)^3} \int_0^{2\pi} d\phi \int_{-1}^{+1} d\cos\theta \frac{2\pi c}{L_z \omega} \sum_{n_y \in \mathcal{Z}} \delta\left(\frac{L_y \omega}{2\pi c} \sin\theta \sin\phi - n_y \right) \delta(\cos\theta)\, \omega^2\, d\omega \\ & = \frac{L_x L_y}{(2\pi c)^2} \sum_{n_y \in \mathcal{Z}} \frac{2\pi c}{L_y \omega} \int_0^{2\pi} d\phi\, \delta\left(\sin\phi - \frac{2\pi c}{L_y \omega} n_y \right) \omega\, d\omega \\ & = \frac{L_x}{2\pi c} \sum_{n_y \in \mathcal{Z}} \int_0^{2\pi} d\phi\, \delta\left(\sin\phi - \frac{2\pi c}{L_y \omega} n_y \right)\, d\omega \end{aligned} \tag{2.10}$$

To calculate the integral over ϕ, the integration interval is first changed into $[-\pi/2, 3\pi/2]$ and then split into two parts :

$$\begin{aligned}
\int_0^{2\pi} d\phi\, \delta\left(\sin\phi - \frac{2\pi c}{L_y\omega} n_y\right) &= \\
& \int_{-\frac{\pi}{2}}^{\frac{\pi}{2}} d\phi\, \delta\left(\sin\phi - \frac{2\pi c}{L_y\omega} n_y\right) + \int_{\frac{\pi}{2}}^{\frac{3}{2}\pi} d\phi\, \delta\left(\sin\phi - \frac{2\pi c}{L_y\omega} n_y\right) \\
&= \int_{-1}^{1} d\sin\phi \frac{\delta\left(\sin\phi - \frac{2\pi c}{L_y\omega} n_y\right)}{\cos\left(\arcsin\left(\sin\phi\right)\right)} - \int_{-1}^{1} d\sin\phi \frac{\delta\left(\sin\phi - \frac{2\pi c}{L_y\omega} n_y\right)}{\cos\left(\pi - \arcsin\left(\sin\phi\right)\right)} \\
&= 2\int_{-1}^{1} dx \frac{\delta\left(x - \frac{2\pi c}{L_y\omega} n_y\right)}{\cos\left(\arcsin x\right)} \\
&= \begin{cases} \frac{2}{\sqrt{1-\left(\frac{2\pi c}{L_y\omega}\right)^2 {n_y}^2}} & \text{if } \left|\frac{2\pi c}{L_y\omega} n_y\right| \le 1 \\ 0 & \text{otherwise} \end{cases}
\end{aligned} \tag{2.11}$$

This gives the final result

$$g(\omega)\, d\omega = \frac{L_x}{\pi c}\left(1 + \sum_{n=1}^{\lfloor\left|\frac{L_y\omega}{2\pi c}\right|\rfloor} \frac{2}{\sqrt{1 - \left(\frac{2\pi c}{L_y\omega}\right)^2 n^2}}\right) \tag{2.12}$$

This equation is checked by Monte Carlo simulation in section 2.3.

In the rest of this chapter, the discreteness of k_y will *not* be taken into account. Only the discreteness of k_z will be taken into account because in the experiments described in Chapters 3 and 4 the effects of the discreteness of k_y are too small to play a role of importance. (With $L_y = 0.1$ mm, the discrete steps in k_y are sized $\frac{2\pi}{L_y} = 63\,\mathrm{m}^{-1}$, which corresponds to (with $c = 3390\,\mathrm{m\,s}^{-1}$) an energy of $E = \hbar c k_y = 2.3 \cdot 10^{-29}$ J. This is small compared to the thermal energy at $T = 1$ K, $E = k_B T = 1.4 \cdot 10^{-23}$ J).

2.2.6 The density of states over θ

The density of states over θ (i.e. the number of phonon states with θ between θ and $\theta + d\theta$) is calculated by integrating $g(\omega, \theta, \phi)$ with respect to ω and ϕ. Only values of $\vec{k}$ with $\omega_{\vec{k}}$ smaller than a given Ω will be taken into account, because the modes will be occupied with a Bose-Einstein distribution, which doesn't allow a noticable number of phonons above a certain energy. The Bose-Einstein distribution will be used in section 2.4 to calculate the equilibrium occupation of the phonon state at a given temperature and hence the heat flux. In the following treatment the case $\theta = \pi/2$, phonons with $k_z = 0$ will be excluded. This case will be examined at the end of this section.

$$\begin{aligned}
g_\Omega(\theta)\, d\theta &= \int_0^\Omega d\omega \int_0^{2\pi} d\phi\; g(\omega, \theta, \phi)\, d\theta \\
&= \int_0^\Omega d\omega \int_0^{2\pi} d\phi\, \frac{L_x L_y L_z}{(2\pi c)^3} \cdot \sum_{n\in\mathcal{Z}} \delta\left(\frac{L_z\omega}{2\pi c}\cos\theta - n\right) \cdot \omega^2 \sin\theta\, d\theta \\
&= \frac{L_x L_y L_z}{(2\pi)^2 c^3} \sin\theta \cdot \sum_{n\in\mathcal{Z}} \int_0^\Omega d\omega \left|\frac{2\pi c}{L_z\cos\theta}\right| \delta\left(\omega - \frac{2\pi c}{L_z\cos\theta} \cdot n\right) \omega^2\, d\theta
\end{aligned}$$

$$= \frac{L_x L_y}{2\pi c^2} \cdot \frac{\sin\theta}{|\cos\theta|} \cdot \sum_{n\in\mathcal{Z}} \int_0^\Omega d\omega\, \delta\left(\omega - \frac{2\pi c}{L_z\cos\theta}\cdot n\right)\omega^2\, d\theta \tag{2.13}$$

The integral in this last equation will yield ω_n^2 with

$$\omega_n = \frac{2\pi c}{L_z \cos\theta}\cdot n$$

provided

$$\omega_n \in [0, \Omega]$$

For $\cos\theta > 0$ it follows

$$n \in \left[0, \frac{\Omega L_z \cos\theta}{2\pi c}\right] \cap \mathcal{Z}$$

and for $\cos\theta < 0$

$$n \in \left[\frac{\Omega L_z \cos\theta}{2\pi c}, 0\right] \cap \mathcal{Z}$$

This yields that

$$\begin{aligned} g_\Omega(\theta)\, d\theta &= \frac{L_x L_y}{2\pi c^2}\cdot\frac{\sin\theta}{|\cos\theta|}\cdot\sum_{n=0}^{\lfloor|\frac{\Omega L_z\cos\theta}{2\pi c}|\rfloor}\left(\frac{2\pi c}{L_z\cos\theta}\right)^2\cdot n^2\, d\theta \\ &= \frac{L_x L_y}{2\pi c^2}\cdot\frac{\sin\theta}{|\cos\theta|}\cdot\left(\frac{2\pi c}{L_z\cos\theta}\right)^2\sum_{n=0}^{\lfloor|\frac{\Omega L_z\cos\theta}{2\pi c}|\rfloor} n^2\, d\theta \end{aligned}$$

Because $\sum_{k=0}^{n} k^2 = \frac{1}{6}n(2n^2+3n+1)$ our final result is

$$g_\Omega(\theta)\, d\theta = \frac{L_x L_y}{{L_z}^2}\cdot\frac{\sin\theta}{|\cos^3\theta|}\cdot\frac{\pi}{3}n(2n^2+3n+1)\, d\theta \text{ with } n = \lfloor|\tfrac{\Omega L_z\cos\theta}{2\pi c}|\rfloor \tag{2.14}$$

This distribution is presented in Figure 2.5 (solid line). Note that if $\Omega < 2\pi c/L_z$ then $n = 0$ so $g_\Omega(\theta)\, d\theta = 0$ for all $\theta \neq \pi/2$. This means that there are no modes with energy $\hbar\omega < 2\pi c\hbar/L_z$ that have a component in the k_z-direction. Recalling the example in Figure 2.1, $\omega < 2\pi c/L_z$ means that the sphere gets smaller than the spacing between the planes and does not have an intersection with other planes than $k_z = 0$.

Also note that the preceding treatment is only valid for $\theta \neq \frac{\pi}{2}$, because then $\cos\theta = 0$. Of course there are a lot of possible modes with θ *exactly* equal to $\frac{\pi}{2}$, since this corresponds with the $k_z = 0$–plane. The number of modes with $\theta = \frac{\pi}{2}$, $N_{\omega<\Omega;\theta=\frac{\pi}{2};0\leq\phi\leq 2\pi}$, can be calculated as follows:

$$\begin{aligned} N &= \lim_{\Delta\to 0}\int_0^\Omega d\omega \int_{\frac{\pi}{2}-\Delta}^{\frac{\pi}{2}+\Delta} d\theta \int_0^{2\pi} d\phi\, \frac{L_x L_y L_z}{(2\pi c)^3}\cdot\sum_{n\in\mathcal{Z}}\delta\left(\frac{L_z\omega}{2\pi c}\cos\theta - n\right)\cdot\omega^2\sin\theta \\ &= \lim_{\Delta\to 0}\int_0^\Omega d\omega \frac{L_x L_y L_z}{4\pi^2 c^3}\cdot\sum_{n\in\mathcal{Z}}\left|\frac{2\pi c}{L_z\omega}\right|\int_{\frac{\pi}{2}-\Delta}^{\frac{\pi}{2}+\Delta} d\theta\, \delta\left(\cos\theta - \frac{2\pi c}{L_z\omega}\cdot n\right)\cdot\omega^2\sin\theta \end{aligned}$$

$$
\begin{aligned}
&= \lim_{\Delta\to 0}\int_0^{\Omega} d\omega \frac{L_x L_y}{2\pi c^2}\cdot \sum_{n\in\mathcal{Z}} \int_{\cos\left(\frac{\pi}{2}-\Delta\right)}^{\cos\left(\frac{\pi}{2}+\Delta\right)} d\cos\theta\,\delta\left(\cos\theta - \frac{2\pi c}{L_z\omega}\cdot n\right)\cdot\omega \\
&= \int_0^{\Omega} d\omega \frac{L_x L_y}{2\pi c^2}\cdot\omega \\
&= \frac{L_x L_y}{4\pi c^2}\cdot\Omega^2
\end{aligned}
\tag{2.15}
$$

Equations 2.14 and 2.15 will also be checked with a Monte Carlo-simulation in section 2.3.

If the classical phonon distribution function of Equation 2.9 is used, calculation of the density of states over θ gives

$$
\begin{aligned}
g_{\Omega,\mathrm{class}}(\theta)\,d\theta &= \int_0^{\Omega} d\omega \int_0^{2\pi} d\phi\; g_{\mathrm{class}}(\omega,\theta,\phi)\,d\theta \\
&= \int_0^{\Omega} d\omega \int_0^{2\pi} d\phi\; \frac{L_x L_y L_z}{(2\pi)^3}\cdot\frac{\omega^2}{c^3}\,\sin\theta\,d\theta \\
&= \frac{L_x L_y L_z}{(2\pi)^2 c^3}\cdot\frac{\Omega^3}{3}\sin\theta\,d\theta
\end{aligned}
\tag{2.16}
$$

Taking the $L_z \to \infty$ limit of Equation 2.14 gives the same result.

2.3 Monte Carlo simulations

The idea of using Monte Carlo techniques to check our calculations was first conceived after finding Equation 2.4 and its unexpected discontinuities. It was decided to generate a large number of phonon $\vec{k}$-vectors of the form $\vec{k} = (k_x, k_y, k_z)$ with $k_i = \frac{2\pi}{L_i} n_i$ and to choose a random integer number in the range $-\frac{N_i}{2} \ldots \frac{N_i}{2}$ for each n_i (see section 2.2.1). With a large number of such random $\vec{k}$-vectors, a good approximation of the phonon distribution function $\mathrm{g}(\omega, \theta, \phi)$ will be generated. Next, all these $\vec{k}$-vectors can be classified with respect to their values of ω, θ and ϕ to generate, for instance, the density of states over ω.

In figures 2.2 to 2.4, $g(\omega)$ from these Monte Carlo simulations is plotted against ω. The material properties have been chosen to resemble a gold strip of dimensions 30 mm $\times$ 0.1 mm $\times$ 100 nm with $c = 3390\,\mathrm{m\,s^{-1}}$ and $a = 0.257\,\mathrm{nm}$. The three figures plot the same function but on a different ω-scale: Figure 2.2 for $\omega < 10^{14}\,\mathrm{s}^{-1}$, Figure 2.3 for $\omega < 10^{12}\,\mathrm{s}^{-1}$ and Figure 2.4 for $\omega < 10^{9}\,\mathrm{s}^{-1}$. In Figure 2.2, it is demonstrated that, for $\omega \gg c\frac{2\pi}{L_z}$ but $\omega < c\frac{\pi}{a}$ Monte Carlo simulation gives the same results for $g(\omega)$ as the classical result of equation 2.2. For $\omega > c\frac{\pi}{a}$ the finite crystal dimensions that the classical approximation does not take into account causes a breakdown of $g(\omega)$. In Figure 2.3 the discrete steps of Equation 2.4 can be seen both in the analytical results and in the Monte Carlo simulation. In Figure 2.4, on an even smaller scale, the discontinuities of Equation 2.12 are shown to comply with the Monte Carlo simulation.

In figure 2.5, the distribution function over theta $g_\Omega(\theta)$ is plotted. An upper limit $\Omega = 1\cdot 10^{12}\,\mathrm{s}^{-1}$ was used. The figure shows the correspondence between Equation 2.14 and the Monte Carlo simulation. The number of modes with $\theta = \pi/2$ also agrees with the analytical result from Equation 2.15.

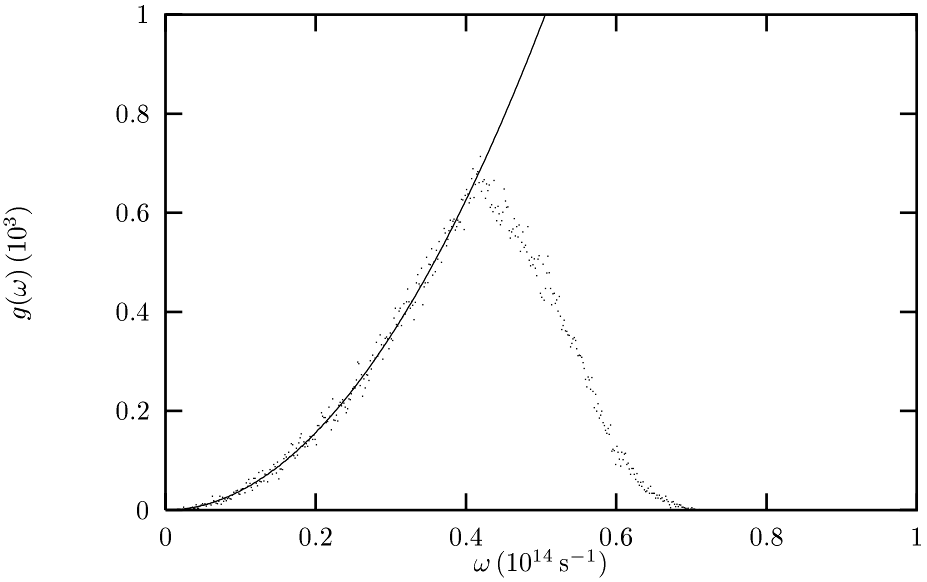

Figure 2.2: Distribution function over ω for $\omega < 10^{14}\,\mathrm{s}^{-1}$. Solid line: Classical function (Equation 2.2), coinciding with the new phonon distribution function (Equation 2.4). points: Monte Carlo simulation

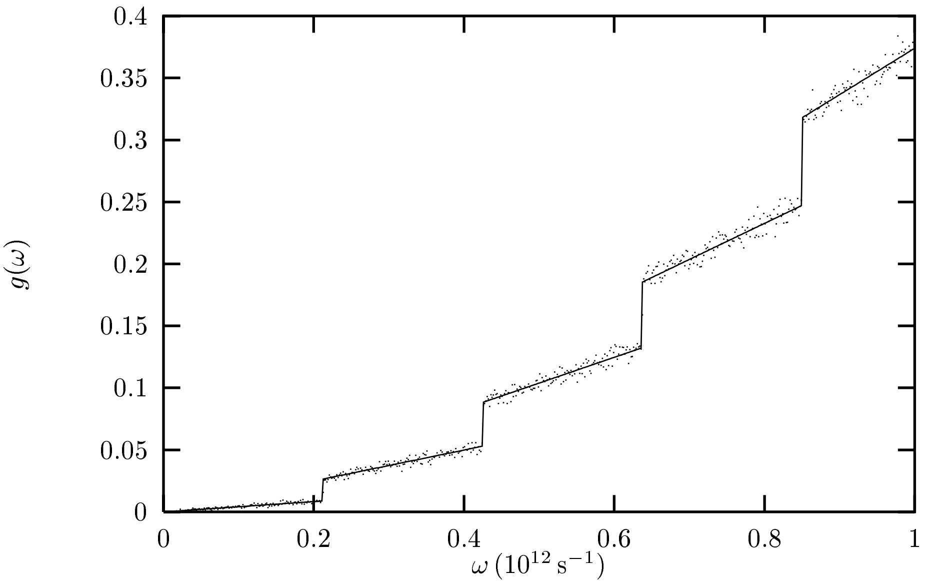

Figure 2.3: Distribution function over ω for $\omega < 10^{12}\mathrm{s}^{-1}$. Solid line: Taking into account discreteness of k_z (equation 2.4); points: Monte Carlo simulation

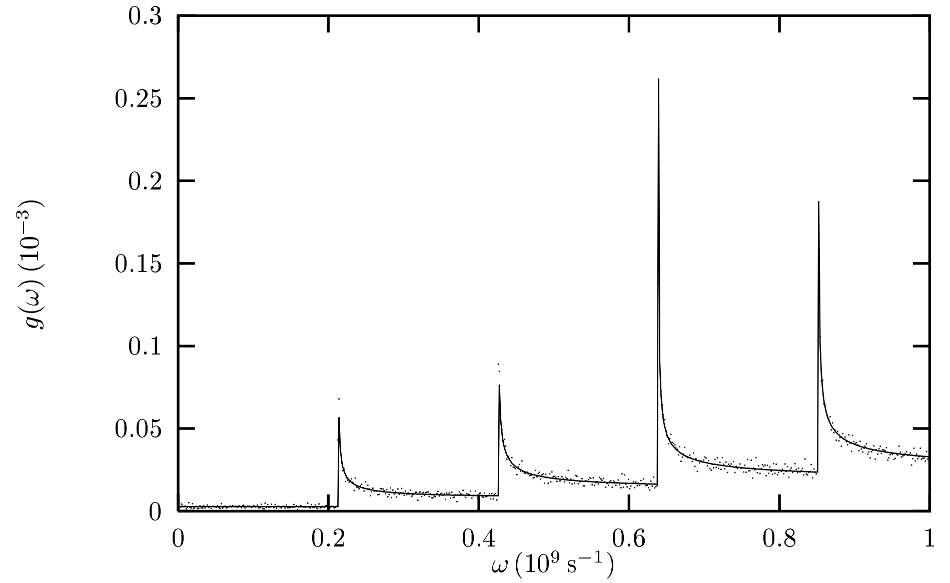

Figure 2.4: Distribution function over ω for $\omega < 10^9\,\mathrm{s}^{-1}$. Solid line: Analytical, taking into account discreteness of k_z and k_y (equation 2.12); points: Monte Carlo simulation

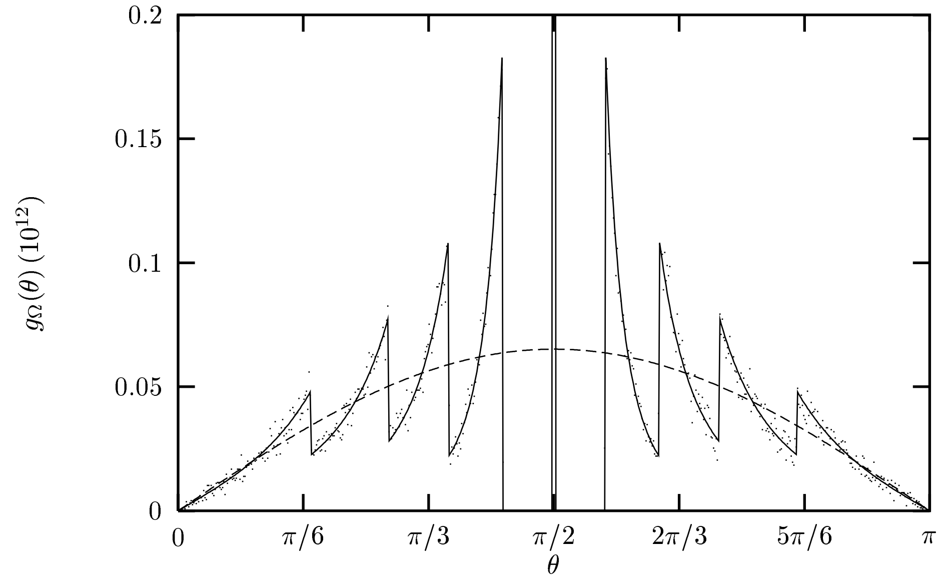

Figure 2.5: Distribution function over θ for $\omega < 10^{12}\mathrm{s}^{-1}$. Solid line: Analytical (Equation 2.14); dashed line: Classical results (Equation 2.16); points: Monte Carlo simulation

2.4 Kapitza resistance

In the experiments described in Chapter 4 a thin gold heater of approx. 100 nm thickness and surface dimensions 0.1 mm $\times$ 30 mm, sputtered on a glass substrate, was used to excite a third sound wave in a Helium film. In this section the effects of the new phonon distribution function on the heat flux $\dot{Q}$ through the gold-glass interface will be considered. Hereafter the new distribution function will be used to recalculate the thermal (Kapitza) resistance.

2.4.1 Heat flux

The expression for the heat flux from a thin heater of dimensions $V = L_x \times L_y \times L_z$, with the interface to the substrate in the z-direction, is (from [12])

$$\dot{Q} = A \cdot \int_0^{\infty} d\omega \int_0^{\frac{\pi}{2}} d\theta \int_0^{2\pi} d\phi \, \frac{g(\omega,\theta,\phi)}{V} \cdot f_{BE}\left(\beta\hbar\omega\right) \cdot \hbar\omega \cdot c \cdot \cos\theta \cdot \alpha(\theta) \tag{2.17}$$

with

$$\begin{aligned}
A &= L_x \cdot L_y \\
f_{BE}(x) &= \frac{1}{e^x - 1} \\
\beta &= \frac{1}{k_B T} \\
k_B &= \text{Boltzmann's constant} \\
T &= \text{thermodynamic temperature of the crystal} \\
\hbar &= \text{Dirac's constant} \\
\alpha(\theta) &= \text{fraction of phonons, coming in at an angle } \theta, \\
& \text{ that cross the interface (see [11])}
\end{aligned}$$

Filling in the phonon distribution function (eq. 2.7) yields

$$\begin{aligned}
\dot{Q} &= \frac{\hbar A}{(2\pi c)^2} \int_0^{\frac{\pi}{2}} d\theta \, \alpha(\theta) \sin\theta \cos\theta \cdot \sum_{n \in \mathcal{Z}} \int_0^{\infty} d\omega \, \frac{\omega^3}{e^{\beta\hbar\omega} - 1} \, \delta\left(\frac{L_z \omega}{2\pi c} \cos\theta - n\right) \\
&= \frac{\hbar A}{2\pi c L_z} \int_0^{\frac{\pi}{2}} d\theta \, \alpha(\theta) \sin\theta \cdot \sum_{n \in \mathcal{Z}} \int_0^{\infty} d\omega \, \frac{\omega^3}{e^{\beta\hbar\omega} - 1} \, \delta\left(\omega - \frac{2\pi c}{L_z \cos\theta} \cdot n\right) \\
&= \frac{\hbar A}{2\pi c L_z} \int_0^{\frac{\pi}{2}} d\theta \, \alpha(\theta) \sin\theta \cdot \sum_{n=1}^{\infty} \frac{{\omega_n}^3}{e^{\beta\hbar\omega_n} - 1} \quad \text{with } \omega_n = \tfrac{2\pi c}{L_z \cos\theta} \cdot n
\end{aligned}$$

Here ω_n is the frequency of a phonon, coming in at an angle θ, with k_z on the n-th k_z-plane. If the dimensionless function $\xi(\theta)$ is defined to be $\frac{2\pi\beta\hbar c}{L_z \cos\theta} = \frac{\beta\hbar\omega_n}{n}$, the energy spacing (relative to $k_B T$) between the phonon modes with the same θ but with different k_z, then

$$\dot{Q} = \frac{(2\pi c)^2 \hbar A}{L_z^4} \cdot \int_0^{\frac{\pi}{2}} d\theta \, \alpha(\theta) \frac{\sin\theta}{\cos^3\theta} \sum_{n=1}^{\infty} \frac{n^3}{e^{\xi(\theta) n} - 1} \tag{2.18}$$

Note that the case $\theta = \pi/2$ causes us no trouble now, because the phonons with $k_z = 0$ don't contribute to the heat flux. In the classical limit, $L_z \to \infty$ or $T \to \infty$ so $\xi \to 0$ and $\sum_{n=0}^{\infty} \to \int_0^\infty dn$,

$$\begin{aligned}\dot{Q} &\approx \frac{(2\pi c)^2 \hbar A}{L_z^4} \cdot \int_0^{\frac{\pi}{2}} d\theta\, \alpha(\theta) \frac{\sin\theta}{\cos^3\theta} \cdot \xi(\theta)^{-4} \int_0^\infty dx\, \frac{x^3}{e^x - 1} \\ &= \frac{\pi^2 k_B^4 T^4 A}{60\hbar^3 c^2} \cdot \int_0^{\frac{\pi}{2}} d\theta\, \alpha(\theta) \sin\theta \cos\theta \qquad (2.19)\end{aligned}$$

which corresponds to the results of Khalatnikov[11] and Little[12].

2.4.2 Kapitza resistance

Because the heat flux in the classical limit is proportional to AT^4, Equation 2.19 can be rewritten for the heat flux from the heater to the substrate to

$$\dot{Q} = \frac{A}{4R_K} \cdot T^4 \qquad (2.20)$$

with R_K the Kapitza resistivity. With the principle of detailed balance it can be concluded that the balance heat flux from the heater (temperature T_H) to the substrate (temperature T_L) equals

$$\dot{Q} = \frac{A}{4R_K} \left({T_H}^4 - {T_L}^4\right) \qquad (2.21)$$

For small temperature difference $\Delta T = T_H - T_L$, $\Delta T \ll T_L$, the thermal resistance become

$$R_{class} \equiv \frac{\Delta T}{\dot{Q}} = \frac{R_K}{AT^3} \qquad (2.22)$$

so that the thermal resistance is proportional to T^{-3}. Using the new phonon distribution function, a thermal resistance, implied in equation 2.18, can also be defined:

$$R \equiv \frac{\Delta T}{\dot{Q}} = \left(\frac{d\dot{Q}}{dT}\right)^{-1} \qquad (2.23)$$

In figure 2.6, the thermal resistance is plotted against the temperature, both for the "classical" results of equation 2.22 and using equation 2.23. In this figure, the fraction α is assumed to be (from [12])

$$\alpha_1(\theta_1) = \frac{\frac{4\rho_2 c_2}{\rho_1 c_1} \cdot \frac{\cos\theta_2}{\cos\theta_1}}{\left(\frac{\rho_2 c_2}{\rho_1 c_1} + \frac{\cos\theta_2}{\cos\theta_1}\right)^2} \qquad (2.24)$$

with

$$\begin{aligned}\frac{\sin\theta_1}{c_1} &= \frac{\sin\theta_2}{c_2}, \text{ Snell's law} \\ \rho_1 &= 19.7 \cdot 10^3\,\mathrm{kgm^{-3}}, \text{ the density of the film material (gold)} \\ \rho_2 &= 2.32 \cdot 10^3\,\mathrm{kgm^{-3}}, \text{ the density of the substrate material (glass)} \\ c_1 &= 3390\,\mathrm{m\,s^{-1}}, \text{ the speed of sound in gold} \\ c_2 &= 5640\,\mathrm{m\,s^{-1}}, \text{ the speed of sound in glass}\end{aligned}$$

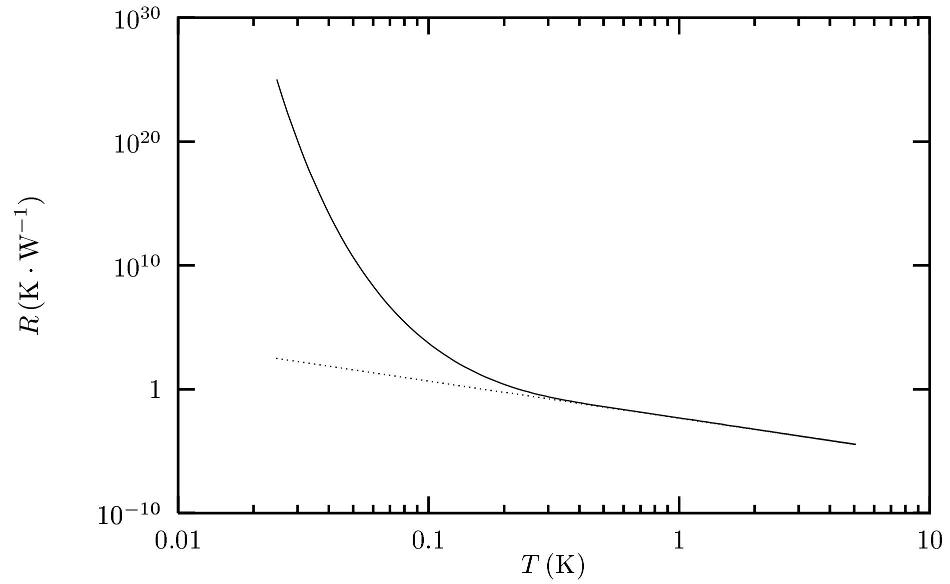

Figure 2.6: Thermal resistance R (Kapitza resistance) between 100 nm thick gold heater and glass substrate as a function of T. Dotted line: According to equation 2.22 (classical T^{-3} law); Solid line: According to equation 2.23 (Taking into account discreteness of k_z)

2.5 Discussion

The new phonon distribution function presented in Equation 2.7 correctly defines the phonon distribution for a thin film as described in section 2.2.1. For temperatures below (typically) 1 K the new distribution function results in a dramatical increase in the Kaptiza resistance between the film (or heater) and an underlying bulk material (or substrate) (Figure 2.6). A physical explanation for this result comes from the discreteness of the values of k_z introduced in the new phonon distribution function. When phonons can have only discrete values of k_z ($k_z = n_i \cdot 2\pi/L_z$, Section 2.2.2), phonons with $k_z \neq 0$ will have an energy of at least $\hbar\omega = \hbar ck = 2\pi c\hbar/L_z$. With thin films (small L_z) and low temperatures ($k_B T \ll 2\pi c\hbar/L_z$), phonons with $k_z \neq 0$ will not be excited, so only phonons with $k_z = 0$ will be present. Phonons with $k_z = 0$ do not contribute to the heat transfer from the heater to the surface, because they do not cause atoms to move in the z-direction. This means that if mostly phonons with $k_z = 0$ are present, the heat transfer will decrease dramatically with decreasing temperature.

2.5.1 Experimental support

In the experimental setup described in Section 3.5 the heater is not in direct contact with the substrate, because it is sputtered onto a thin Kapton foil which is glued to a copper substrate (Figure 3.7). In this case there are two extra layers between the heater and the substrate (Kapton and Stycast 1266 glue). Because these layers will be at a lower temperature than the heater, their Kapitza resistance will be higher. If this effect occurs, the heat leak from the heater to the substrate will be low compared to the “classical” case where the effects of the new phonon distribution are not taken into account. This means that more heat will be delivered to the ^{4}He film, making third sound excitation easier!

Mester et.al. [13] describe experiments on heat transport between solids and superfluid ^{4}He films. In these experiments the heat flux is dissipated by evaporation of ^{4}He atoms. They find a giant effective Kapitza resistance (3 orders of magnitude greater than for bulk helium), but no dependence of the Kapitza resistance on film thickness. This indicates that the phonon distribution as described in this chapter is not responsible for the giant Kapitza resistance found by Mester since the Kapitza resistance depends on the heat flux (Equation 2.23) which in turn depends on film thickness L_z (Equation 2.18).

Eggenkamp [8, p. 32] found an increasing thermal resistance between a gold heater film and a ^{4}He film for temperatures below 0.60 K. Here evaporation and third sound are the dissipation mechanisms. Eggenkamp found a thickness dependence of the heat transport, although only 2.5 a.l. and 1.9 a.l. films were studied. However, Eggenkamps experiments describe heat transport from a gold heater film to a superfluid ^{4}He film. The theory presented in this chapter is able to describe the phonon distribution in the heater, but it is not able to describe the heat transfer from the heater to the ^{4}He film.

2.5.2 Suggestions for improvement

In this chapter only longitudinal phonon modes of a cubic lattice are considered. This model should be extended to other lattices and other phonon polarizations. Quantum effects due to the small dimensions of the gold film should be taken into account as well. For instance, quantum tunneling of phonons through the interface could play a role. Excitations in superfluid ^{4}He films (phonons *and* rotons) should be considered in order to be able to apply this model to the experiments of Eggenkamp and to the experiments described in Chapter 4.

Chapter 3

Experimental set-up

3.1 Cryogenics

Third sound experiments with ^{4}He have to be done at temperatures around or below 1.3 K, because otherwise third sound is strongly attenuated due to the ^{4}He vapour. To reach 1.3 K, a pumped ^{4}He cryostat is used (Figure 3.1). It consists of a set of stainless steel vessels placed inside each other. The outermost is vacuum, the one inside it is filled with liquid nitrogen at 77 K. Inside the nitrogen vessel there is a vacuum vessel again and the innermost vessel is filled with liquid helium. The vapour in this vessel is pumped away to reach a minimum temperature of about 1.19 K. The experimental cell is hanging in this helium bath.

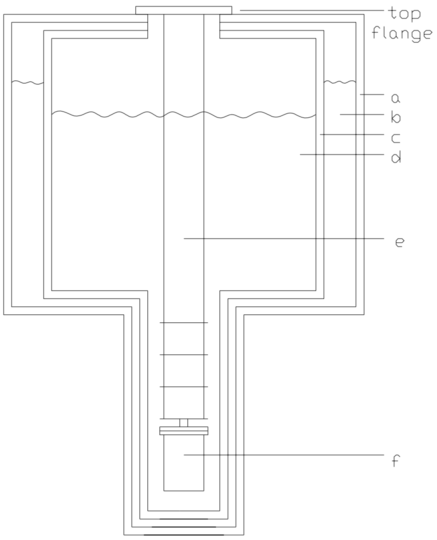

Figure 3.1: Pumped ^{4}He cryostat. a. Vacuum chamber b. Nitrogen bath c. Vacuum chamber d. Helium bath e. Insert f. Cell

3.2 The cell

The copper cell made by Pinkse [14] was used in the experiments. It has enough space for a $(10.8 \pm 0.6)\mathrm{m}^2$ copper sinter, also made by Pinkse. The sinter is needed to stabilize the ^{4}He film thickness inside the cell and thermally anchor the film to the cell. The cell also features a feedthrough for electrical wiring of which 19 connections are still usable.

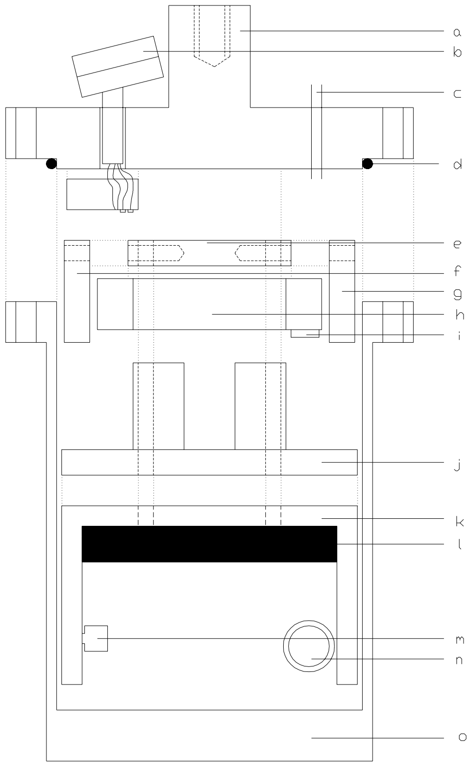

Figure 3.2: Experimental cell. a. Cell top b. Feedthrough c. Filling capillary d. Indium ring e. Bottom plate f. Left frame g. Right frame h. Glass and copper bars i. Thermometers j. Platform k. Sinter holder l. Sinter m. Thermometer n. Pressure gauge o. Cell bottom

A new interior for the cell was designed, capable of holding both a copper and a glass resonator bar at the same time (see Figure 3.2 and detail on front page). The following parts were made for this interior:

- A copper bottom plate, which is screwed to the top flange of the cell (Appendix, figure A.1).
- A copper resonator bar (Appendix, figure A.4).
- A glass resonator bar (Appendix, figure A.5).
- Two frames that together hold both bars (Appendix, figure A.2 and A.3).
- A mounting platform that can be screwed to the bottom plate (Appendix, figure A.6). Pinkse's copper sinter can be screwed to this platform.

The cell also features a sapphire capacitive pressure gauge, hanging in the free space below the sinter, and four resistor thermometers. One thermometer is fitted to the frame, two are glued to both bars and one is hanging in the helium bath.

3.3 The bar geometry

Both bars have a diameter of 10 mm and a length of 30 mm. They are suspended above the (silver–plated copper) bottom plate at distance of about 15 μm for the copper bar and about 32 μm for the glass bar. Both bars feature a mechanism for third sound excitation and third sound detection. Third sound is excited by a heater (H1 and H2 in Figure 3.3) and detected using a detector capacitance (D1 and D2). The excitation and detection mechanism are described in sections 3.5 and 3.6. A third sound wave, excited at one of the heaters, would travel both up and down. The wave that starts moving down would reach the detector after running along a quarter of the bar circumference. After running completely around the bar, it would reach the detector again after 5/4 of the bar circumference, and again at 9/4, 13/4, etc. The wave that starts moving up would reach the detector after 3/4 of the bar circumference, and again at 7/4, 11/4, etc. In this way a signal can be expected at the detector after 1/4, 3/4, 5/4, 7/4, etc. times the time needed to complete one loop around the bar.

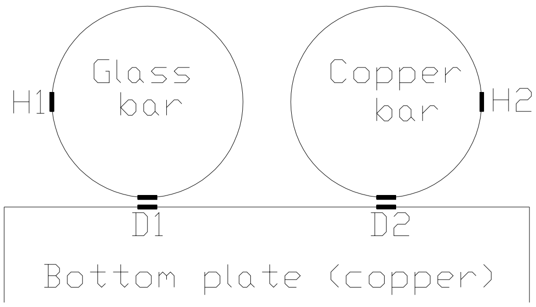

Figure 3.3: Twin bars setup

3.4 Electrolytic polishing of copper

The copper resonator bar needed to be polished in order to have a clean third sound signal. If the surface is rough, the circumference of the cylinder will vary from place to place. This will cause a difference in time needed by a third sound pulse to travel around the cylinder, resulting in a distorted signal. Mechanically polishing copper is very hard, because the material is soft. In this case it is even harder because the item to be polished is a copper *cylinder*. The solution chosen was to use a technique called electrolytic polishing[17]. Electrolytic polishing (or *electropolishing*) provides the following two effects on the surface to be polished:

- "smoothing" of the surface by elimination of the large-scale irregularities (above 1 μm in size)
- "brightening" by removal of the smaller irregularities (down to a around 10 nm).

The item to be polished (in our case the copper cylinder) forms the anode in an electrolytic cell (Figure 3.4). The item is first mechanically polished with sandpaper of successively finer grade (up to 4000). A solution of 70% orthophosphoric acid (H_3PO_4) in water is used as electrolyte. The electric motor rotates the anode (the copper bar) with a frequency of about 1 Hz.

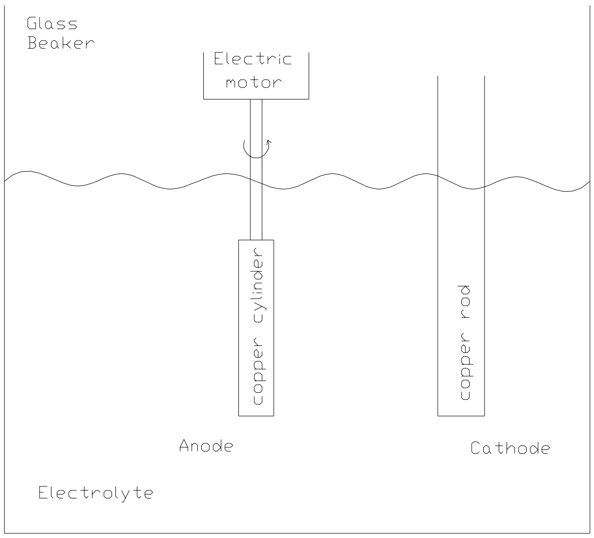

Figure 3.4: Setup for electropolishing the copper bar

The electrical circuit used is presented in Figure 3.5. Here R is a $1\,\Omega$ resistor used to measure the current running through the cell, V_R is the voltage across this resistor, V is the voltage across the cell and $V_T = V_R + V$ is the voltage across the total circuit. By using an X,Y–recorder with V on the X input and V_R on the Y input it is possible to measure the I, V-diagram of the electrolytic cell. A typical I, V-diagram is presented in Figure 3.6. In this diagram a number of stages can be recognised and the procedure for electropolishing is as follows:

1. Start increasing V_T. This causes I to increase. In this stage the anode surface is etched. This results in impairment of the anode surface and should last as short a time as possible.
2. At a certain moment, a blue, translucent viscous layer starts to form on the anode surface. This layer probably consists of copper phosphates. It is this layer that controls the polishing process. The current I will drop because the viscous layer increases the cell resistance. V_T

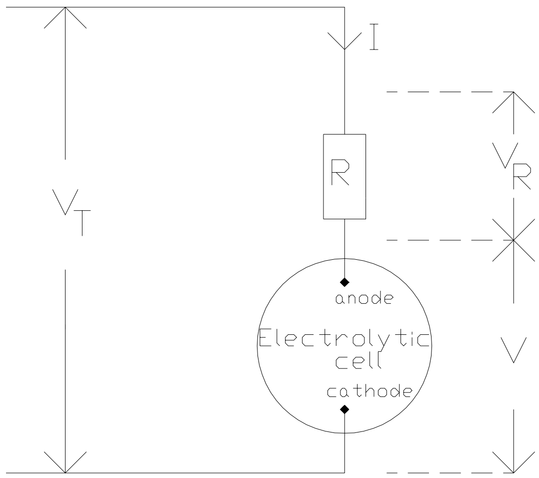

Figure 3.5: Electrical circuit for electropolishing

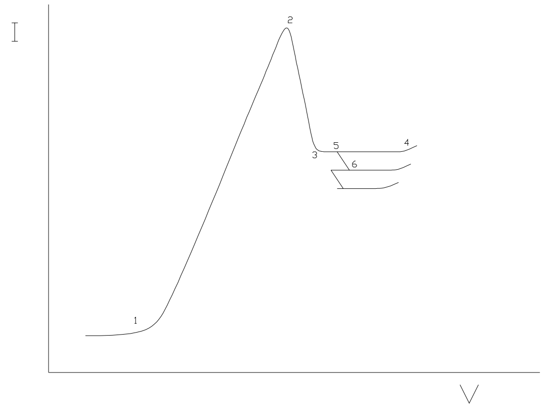

Figure 3.6: Typical electropolishing I, V-diagram

is now held constant. The cell resistance still increases, resulting in a drop of I, a decrease of V_R and consequently an increase of V.

3. When the viscous layer is completed, the current reaches equilibrium. Increasing V_T a little again reveals the "polishing plateau", where I does not depend on V. The viscous layer limits the current. The anode surface is now being polished. Total cell voltage is about 2.5 V. To check this condition, V_T is increased further.
4. If V_T is increased too far the polishing plateau ends. Gas evolution occurs, destroying the viscous layer and pitting the anode surface. The destruction of the viscous layer allows the current to rise again. The total voltage V_T is quickly decreased to avoid pitting.
5. After some time, the current I will decrease again slowly, probably because the viscous layer still grows a little. This decrease of I causes a corresponding rise of V, like at point 2.
6. Increasing V_T reveals the polishing plateau again. Find the end of the plateau to make sure the anode is still being polished and go back.
7. Repeat steps 5 and 6 for about 15 minutes. The item is removed from the electrolyte approximately every 5 minutes for washing with distilled water.

There are a number of practical points to be observed when electropolishing:

- It should be possible to insert and remove the item to be polished quickly from the electrolyte (for washing purposes).
- Either rotate the anode or stir or rotate the electrolyte. This allows fresh electrolyte to reach the anode. Do not rotate too fast, because this may destroy the viscous layer.
- Make sure the item is in contact with the electrolyte only when the required potential difference across the cell is present, since otherwise etching may occur. Use a test piece to determine the appropriate voltage.
- The relative position of the anode to the cathode should remain fixed during the treatment. If this position shows variations, the internal resistance of the cell will also variate, which will make it make difficult to maintain polishing conditions.
- At the cathode, gas evolution will occur. Take care this will not destroy the viscous layer at the anode.
- Remove the item from the electrolyte every 5 minutes, wash with distilled water.
- After polishing, quickly remove the item from the electrolyte and wash with distilled water and alcohol.
- Getting the "feeling" for electropolishing takes some time. First practice on some test pieces and see how they get severely pitted if the voltage gets too high.

The copper bar used in the cell was polished brightly overall, but still has a few pits. Further polishing was not thought to be a good idea because the diameter of the bar had already decreased from 10.0 mm to 9.6 mm as a result of repeated etching and polishing.

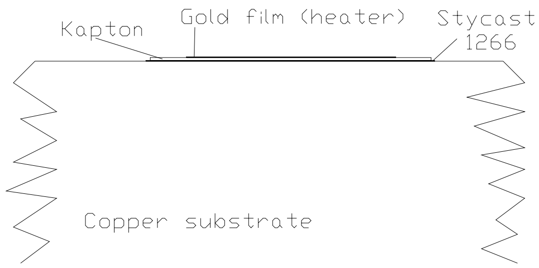

Figure 3.7: Heater on copper

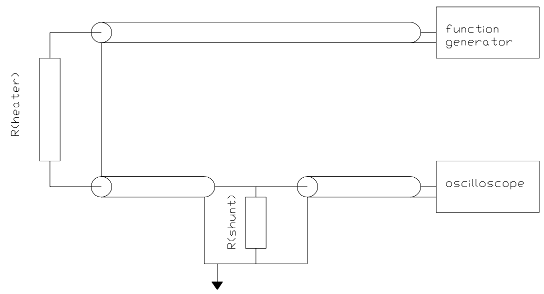

Figure 3.8: Excitation electronics

3.5 Excitation of third sound

Thermal excitation is used to excite a third sound pulse on the bar. A 0.2 mm wide and 30 mm long gold electrode (the "heater") was sputtered on the side of both bars. On the copper bar, a 13 μm thick piece of Kapton foil was first glued to the copper as insulation. The heater was then sputtered on the Kapton (Figure 3.7). By sending one half-sine current pulse through the heater, a third sound pulse can be excited. In Figure 3.8, the excitation electronics are drawn. R_{heater} is measured using a four-point method. The current through the heater can be measured by measuring the voltage across R_{shunt} on the oscilloscope. If that voltage is V, then the current I through the heater equals

$$I = \frac{V}{R_{shunt}}$$

The energy dissipated in the heater in one half-sine equals

$$\begin{aligned} E &= \int_0^{\frac{1}{2f}} R_{heater} \cdot (I \cdot \sin 2\pi f t)^2 \, dt \\ &= \frac{1}{4f} \cdot R_{heater} \cdot I^2 \\ &= \frac{1}{4f} \cdot R_{heater} \cdot \left(\frac{V}{R_{shunt}} \right)^2 \end{aligned}$$

with f the frequency of the half-sine (typically 3 kHz).

3.6 Detection of third sound

In both gaps between the bars and the bottom plate a capacitor was constructed by sputtering 1 mm wide electrodes on the bar and on the bottom plate, where necessary of course insulated by a layer of Kapton. Because of the relative dielectric constant of ^{4}He at 1.3 K, $\varepsilon_r = 1.055$, the capacitance will change when a third sound pulse passes the detector. The detector capacitor C is combined with an inductance L in an LC–oscillator circuit (Figure 3.9). A change in capacitance results in a change in resonant frequency by $\omega^2 LC = 1$. A BD5 tunnel diode is used to drive the oscillator circuit and compensate its losses. The schematics for the tunnel diode oscillator and filtering circuits are also given in Figure 3.9.

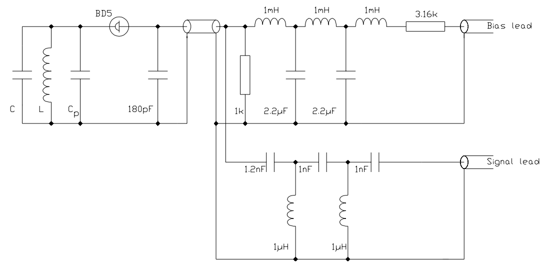

Figure 3.9: Tunnel diode and filtering electronics

These filtering circuits separate the approx. 20 MHz RF signal from the oscillator from the voltage needed to bias the tunnel diode. The RF signal is first amplified with a 30 dB HF amplifier and then mixed down to 70 kHz with a synthesizer sine wave (Figure 3.10. Numbers in this figure are meant as example). This signal is then amplified with a 20 dB, 50-90 kHz amplifier. A frequency counter (HP 5300B) is used to keep track of the TD resonant frequency. Next, the frequency (corresponding to ^{4}He film thickness) is "translated" into a voltage with a P.L.L. (Phase Locked Loop). This signal is amplified 50–200 times (with a Princeton 113 pre-amp) and filtered with a 25 kHz LP-filter to eliminate the 70 kHz (and harmonics) that come from the P.L.L. The resultant signal follows the ^{4}He film thickness change in the detector after a pulse is sent through the heater. This signal is averaged up to 16384 times in a Nicolet 370 signal averager.

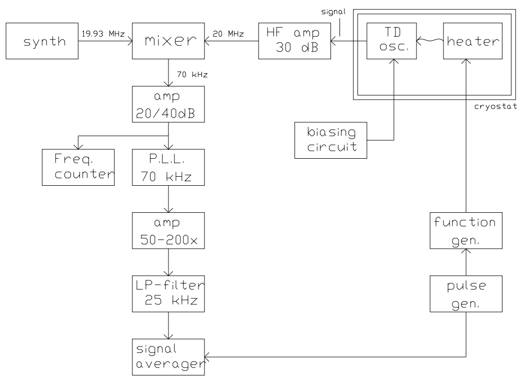

Figure 3.10: Detection system

3.7 Gas handling system

The gas handling system after addition of an extra valve right above the cel is given in Figure 3.11. The extra valve was not present during the experiments described in Chapter 4. v_0 is a calibrated volume used to determine the other volumes. V_{tot} is the volume used to admit ^{4}He gas to the cell.

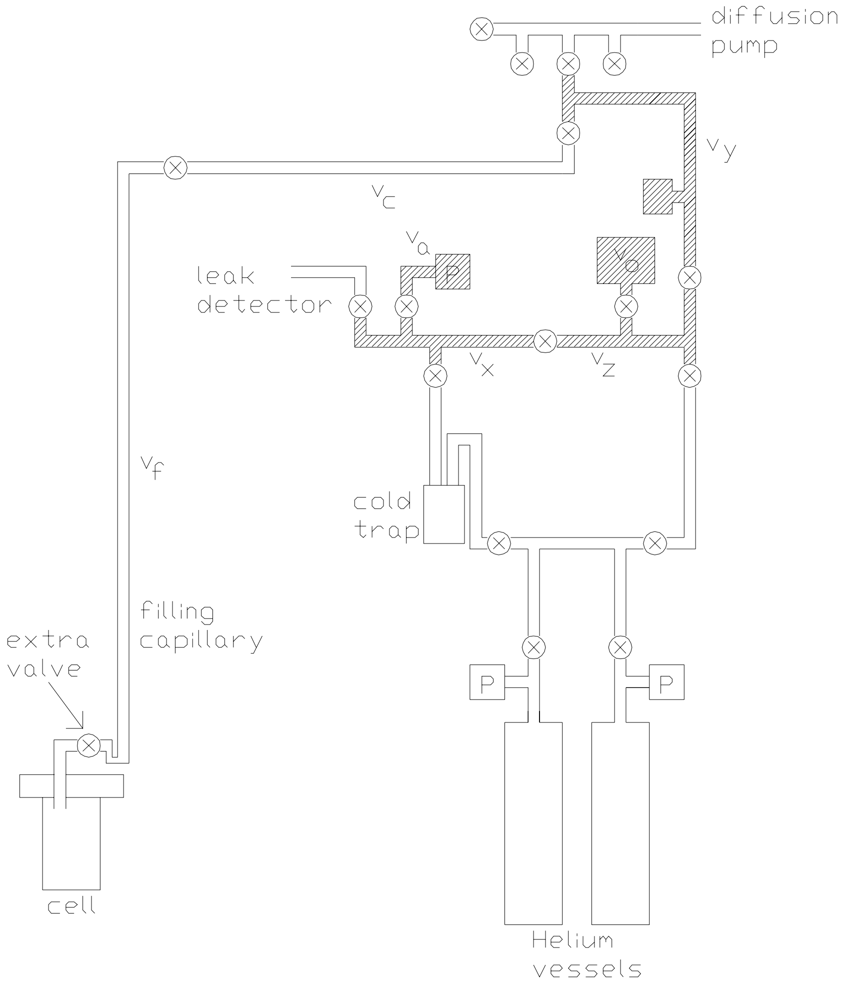

Figure 3.11: Gas handling system. P is a pressure gauge, $v_a = 3.46\,\text{cm}^3$, $v_x = 4.69\,\text{cm}^3$, $v_z = 3.48\,\text{cm}^3$, $v_0 = 31.32\,\text{cm}^3$, $v_y = 39.2\,\text{cm}^3$, $v_c = 32.6\,\text{cm}^3$, $v_f = 37.0\,\text{cm}^3$, $v_{cell} = 112\,\text{cm}^3$. Shaded volume: $V_{\text{tot}} = v_a + v_x + v_z + v_0 + v_y = 81.95\,\text{cm}^3$

Chapter 4

Experimental results

The experiment started by evacuating the cell and cooling down to 1.21 K. During the experiment, the temperature was held at a value of (1.21 ± 0.02) K. After cooldown to 1.21 K, the resonator circuit on the copper bar resonated at 24 MHz. The circuit on the glass bar resonated at 39 MHz. Helium gas was admitted from a room temperature volume $V_{\mathrm{tot}} = 81.95\,\mathrm{cm}^3$ (see Figure 3.11). A certain amount of gas was let into this volume and the pressure was measured. Opening the valves to the cell caused the ^{4}He in the room temperature volume to be sucked into the cell. Closing the valves and repeating the procedure enabled a progressively thicker ^{4}He layer inside the cell. Adding together the pressures of helium in this volume that were admitted gives the accumulated pressure p_{in}, a measure for the number of atoms in the cell. Using the ideal gas law the number of moles ^{4}He in the cell can be found:

$$n_{\mathrm{in}} = \frac{RT}{p_{in} V_{\mathrm{tot}}}$$

with R the ideal gas constant and T the temperature.

For each layer thickness, a large number (up to 16384) excitation pulses were given consecutively on both bars and the resulting detector signals were averaged. Due to interference between both detector circuits, it was not possible to measure on both bars simultaneously. The excitation energy per pulse calculated according to Section 3.5 amounted to $0.11\,\mu$J on the glass bar and to $0.13\,\mu$J on the copper bar.

4.1 Third sound signals

A typical third sound signal on glass (n_{in} = 16.83 mmol) is presented in Figure 4.1. On the horizontal axis is the time after sending the heater pulse. On the vertical axis is the signal as captured by the Nicolet signal averager (Section 3.6). This signal corresponds with the ^{4}He layer thickness at the detector. The first peak seen in the signal is an artifact which originates from interference by the heater pulse. This peak is not seen at time 0 because of delaying effects of the detection electronics. The second peak is the first third sound pulse arriving at the detector. This pulse has travelled 1/4 of the bar circumference (Section 3.3). Up to eight third sound peaks can be seen in the signal. By measuring the mean time between two adjacent peaks the third sound speed can be calculated, using the circumference of the bar, $L = \pi d = \pi \cdot 1.0\,\mathrm{cm} = 3.142\,\mathrm{cm}$ with d the diameter of the bar. The third sound speed on glass $c_{3,gl}$ was in this case $(13.2 \pm 0.8)\,\mathrm{m\,s^{-1}}$. This corresponds to a film thickness of 8.5 atomic layers (using Equation 1.1 and Figure 1.1). 1 atomic layer or a.l. of ^{4}He corresponds to 0.36 nm. On the glass bar, third sound was seen when at least 6.2 mmol ^{4}He was admitted, with a corresponding measured third sound speed $c_{3,gl} = (23.4 \pm 0.9)\,\mathrm{m\,s^{-1}}$ and a calculated film thickness $\delta = 5.6\,$a.l.

In Figure 4.2, the third sound signal on glass with $n_{\mathrm{in}} = 35.9$ mmol ^{4}He in the cell is presented. The third sound speed $c_{3,gl}$ now equals $(5.02 \pm 0.22)\,\mathrm{m\,s^{-1}}$, corresponding to a film thickness of 16.4 a.l. In the plot again first an interference peak, then two clear third sound peaks. After the second peak reflections are seen (e.g. the positive peak at 7.5 ms), making the determination of further peaks problematical. These reflections are probably caused at the detector, where the small gap causes interaction between the ^{4}He films on both electrodes. This interaction can cause a partial reflection of the third sound wave.

A typical third sound signal (at $n_{\mathrm{in}} = 35.9$ mmol) on copper is presented in Figure 4.3. Here six third sound peaks can be distinguished. Third sound speed $c_{3,Cu}$ is now $(4.47 \pm 0.5)\,\mathrm{m\,s^{-1}}$. Under the same conditions, the third sound speed on glass was measured (see above) and was $c_{3,gl} = (5.02 \pm 0.22)\,\mathrm{m\,s^{-1}}$. The ^{4}He film thickness on copper δ_{Cu} was calculated from $c_{3,gl}$ using the method described in the next section and amounted to $\delta_{Cu} = 21\,$a.l. On the copper bar, third sound was seen when at least 28.8 mmol ^{4}He was admitted, with a corresponding third sound speed $c_{3,Cu} = (6.7 \pm 0.4)\,\mathrm{m\,s^{-1}}$. The film thickness on copper, calculating using $c_{3,gl}$, was in that case $\delta_{Cu} = 16.3\,$a.l.

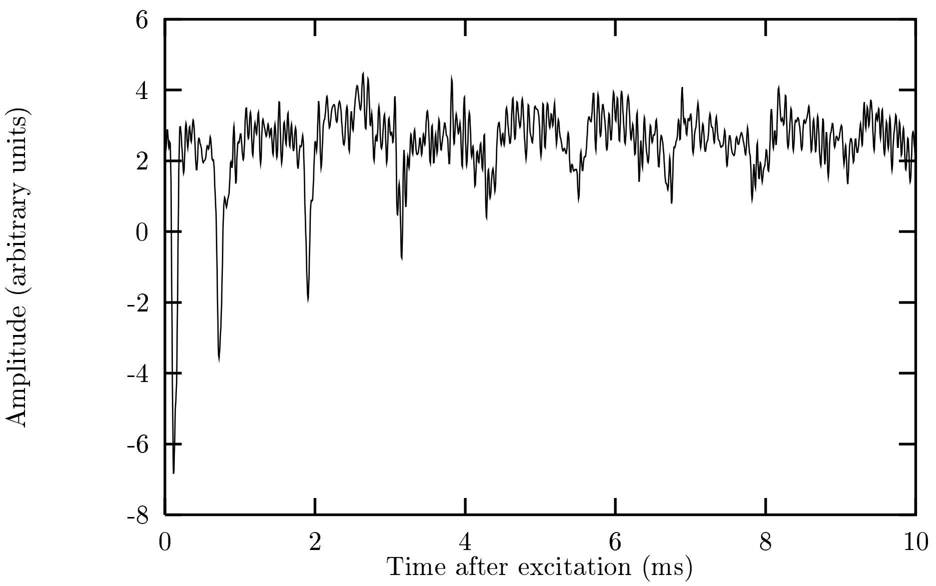

Figure 4.1: Third sound signal on glass. $n_{\mathrm{in}} = 16.83$ mmol. Calculated $c_3 = (13.2 \pm 0.8)\,\mathrm{m\,s^{-1}}$. $\delta_{gl} = 8.5\,$a.l.

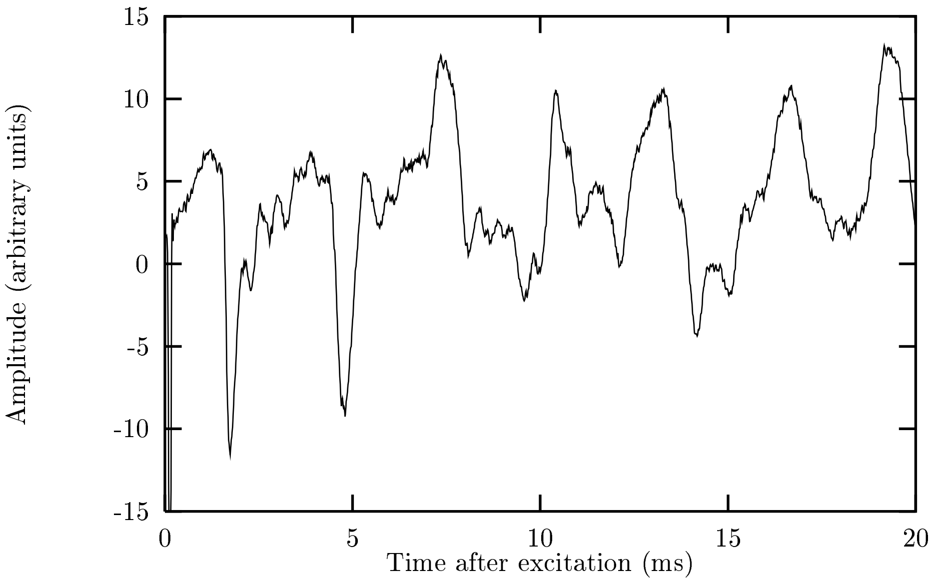

Figure 4.2: Third sound signal on glass. $n_{\text{in}} = 35.9$ mmol. Calculated $c_3 = (5.02 \pm 0.22)\,\mathrm{m\,s^{-1}}$. $\delta_{gl} = 16.4\,\text{a.l.}$

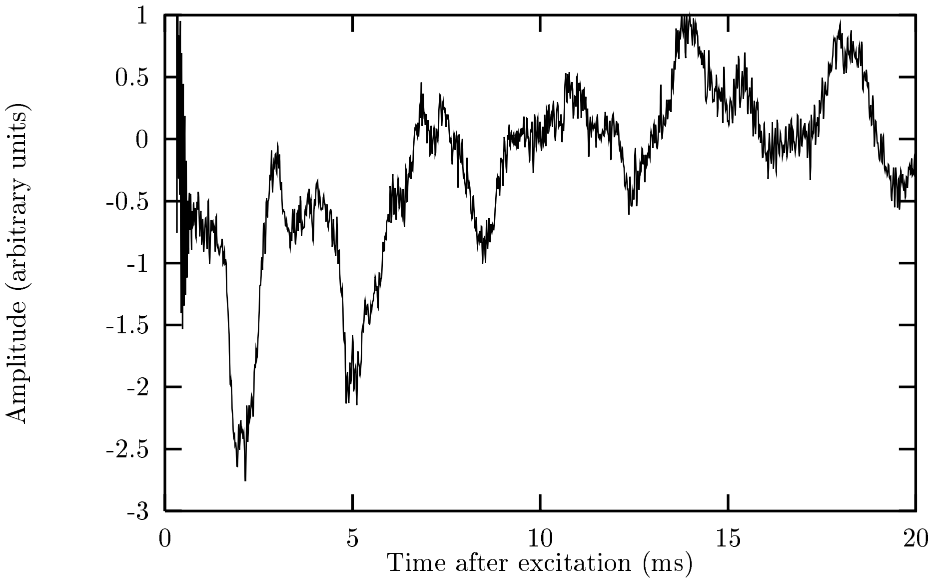

Figure 4.3: Third sound signal on copper. $n_{\text{in}} = 35.9$ mmol. Calculated $c_3 = (4.47 \pm 0.5)\,\mathrm{m\,s^{-1}}$. $\delta_{Cu} = 21\,\text{a.l.}$

4.2 Third sound speed

In Figure 4.4, the measured values of the third sound speed, both on copper and on glass, are plotted against the amount of ^{4}He admitted to the cell, n_{in}. Measurements on copper and on glass at the same value of n_{in} were performed consecutively (within 1 to 12 hours).

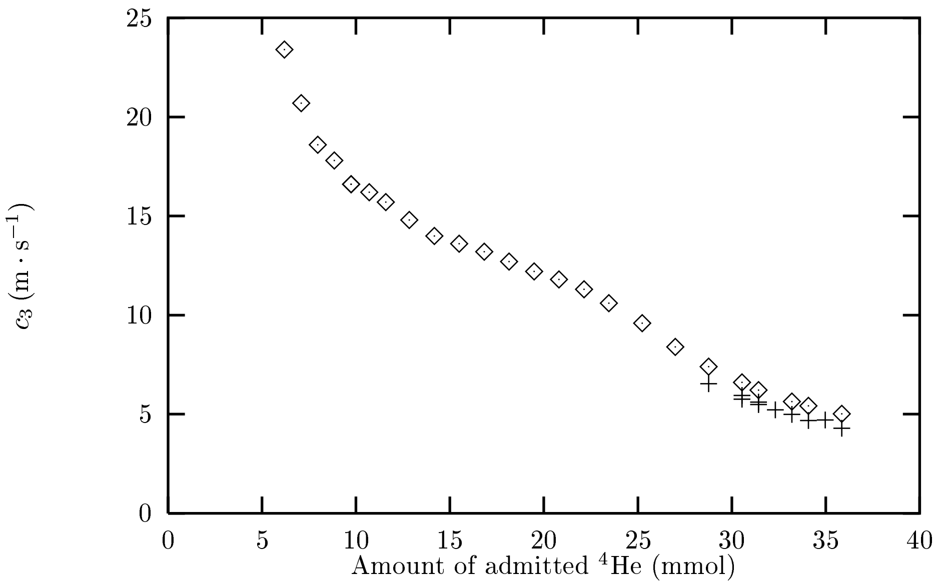

Figure 4.4: Third sound speed c_3 on copper and on glass as a function of the amount of ^{4}He in the cell, n_{in}. $\diamond$ Glass; + Copper

4.2.1 Comparison of $c_{3,gl}$ and $c_{3,Cu}$

In Figure 4.4 the third sound speed on glass $c_{3,gl}$ and the third sound speed on copper $c_{3,Cu}$ at the same value of n_{in} are very close to each other. This can be explained as follows. Both bars are in the same cell, which means that the vapour pressure p_v is the same above both substrates. Using Equation 1.8 it follows that the Van der Waals potential at the film–vapour interface $\Omega(\delta)$ has the same value for the ^{4}He films on the copper and glass bars. The definition of Ω, Equation 1.4 can be approximated by

$$\Omega_{gl} \approx -\frac{\gamma_{gl}}{{\delta_{gl}}^3} \tag{4.1}$$

and

$$\Omega_{Cu} \approx -\frac{\gamma_{Cu}}{{\delta_{Cu}}^3} \tag{4.2}$$

(using $\delta \ll \beta \approx 42\,\mathrm{a.l.}$). Since $\Omega_{\mathrm{gl}} = \Omega_{\mathrm{Cu}}$, δ_{Cu} can be expressed in δ_{gl}:

$${\delta_{Cu}}^3 \approx \frac{\gamma_{Cu}}{\gamma_{gl}}\,{\delta_{gl}}^3 \tag{4.3}$$

Using Equations 1.1 and 1.3 and the approximated expressions for Ω (Equations 4.1 and 4.2) the ratio of the third sound speed on copper and on glass in the same cell can be calculated as follows:

$$\begin{aligned}\frac{{c_{3,gl}}^2}{{c_{3,Cu}}^2} &\approx \frac{\left(\frac{\rho_s}{\rho}\right)_f f_{gl}(\delta_{gl})\,\delta_{gl}}{\left(\frac{\rho_s}{\rho}\right)_f f_{Cu}(\delta_{Cu})\,\delta_{Cu}} = \frac{\frac{3\gamma_{gl}}{{\delta_{gl}}^4}\cdot\delta_{gl}}{\frac{3\gamma_{Cu}}{{\delta_{Cu}}^4}\cdot\delta_{Cu}} \\ &= \frac{\frac{\gamma_{gl}}{{\delta_{gl}}^3}}{\frac{\gamma_{Cu}}{\frac{\gamma_{Cu}}{\gamma_{gl}}{\delta_{gl}}^3}} = 1 \end{aligned} \tag{4.4}$$

Thus $c_{3,gl} \approx c_{3,Cu}$.

4.2.2 Calculation of δ_{gl} and δ_{Cu}

Measurement of $c_{3,gl}$ enables determination of the film thickness on glass and on copper as described below (see also Table 4.1). Using Equation 1.1 the ^{4}He film thickness on glass can be calculated from the third sound speed since γ_{gl} is well know ($2.6\cdot 10^{-24}\,\mathrm{m^5s^{-2}}$). Now the Van der Waals potential Ω can be calculated using Equation 1.4. Because this value is also the Van der Waals potential on the copper bar, the film thickness on copper δ_{Cu} can be calculated by inverting Equation 1.4. The Van der Waals constant on copper, γ_{Cu}, which is needed for this calculation is taken from Brisson[3] ($\gamma_{Cu} = 5.92\cdot 10^{-24}\,\mathrm{m^5s^{-2}}$). Other sources for γ_{Cu} are Pinkse[14] ($\gamma_{Cu} = (2.8\pm 1.4)\cdot 10^{-24}\,\mathrm{m^5s^{-2}}$), Shirron et.al.[16] ($\gamma_{Cu} = (3.09\pm 0.44)\cdot 10^{-24}\,\mathrm{m^5s^{-2}}$), and various theoretical predictions (5.5 to $6\cdot 10^{-24}\,\mathrm{m^5s^{-2}}$), mentioned by Brisson.

Equation 1.1:	$c_{3,gl}$, γ_{gl}	$\rightarrow$	δ_{gl}
Equation 1.4:	δ_{gl}, γ_{gl}	$\rightarrow$	Ω_{gl}
	Ω_{gl}	$=$	Ω_{Cu}
Equation 1.4:	Ω_{Cu}, γ_{Cu}	$\rightarrow$	δ_{Cu}

Table 4.1: Calculating δ_{Cu} from $c_{3,gl}$

4.2.3 $c_{3,Cu}$ versus δ_{Cu}

In Figure 4.5 the measured third sound speed on copper $c_{3,Cu}$ is plotted against the film thickness on copper as calculated from the third sound speed on glass as described in Section 4.2.2 (diamonds). The theoretical relation (Equation 1.1, now for copper) is given in the figure as well (solid line). To calculate δ_{Cu} from the measured $c_{3,gl}$, $\gamma_{Cu} = 5.92 \cdot 10^{-24}\,\mathrm{m^5 s^{-2}}$ (from Brisson[3]) and dead layer thickness $D(T) = 1.91\,$a.l. (from Equation 1.5) were used. The theoretical values of $c_{3,Cu}$ lie 20% higher than the measured values.

The dashes in Figure 4.5 give the theoretical relation for $c_{3,Cu}$ as a function of δ_{Cu} now using $\gamma_{Cu} = 4.3 \cdot 10^{-24}\,\mathrm{m^5 s^{-2}}$ and $D(T) = 1.91\,$a.l. This line seems to agree with the measured values of $c_{3,Cu}$. Note that here δ_{Cu} is calculated from $c_{3,gl}$ using $\gamma_{Cu} = 5.92 \cdot 10^{-24}\,\mathrm{m^5 s^{-2}}$ while the theoretical values of $c_{3,Cu}$ are calculated from δ_{Cu} using $\gamma_{Cu} = 4.3 \cdot 10^{-24}\,\mathrm{m^5 s^{-2}}$. It would be better to use the same value of γ_{Cu} for both calculations, but in that case it is not possible to get a good fit. Better results are obtained if the dead layer thickness $D(T)$ (Section 1.2) is involved in the fitting procedure as well. The + marks in Figure 4.5 represent $c_{3,Cu}$ as a function of δ_{Cu} where $\gamma_{Cu} = 4.3 \cdot 10^{-24}\,\mathrm{m^5 s^{-2}}$ and $D(T) = 5.66\,$a.l. are used. The theoretical relation with these values for γ_{Cu} and $D(T)$ is given as the dots&dashes. Now the measured values for the third sound speed on copper $c_{3,Cu}$ agree within a few % with the theoretical calculations.

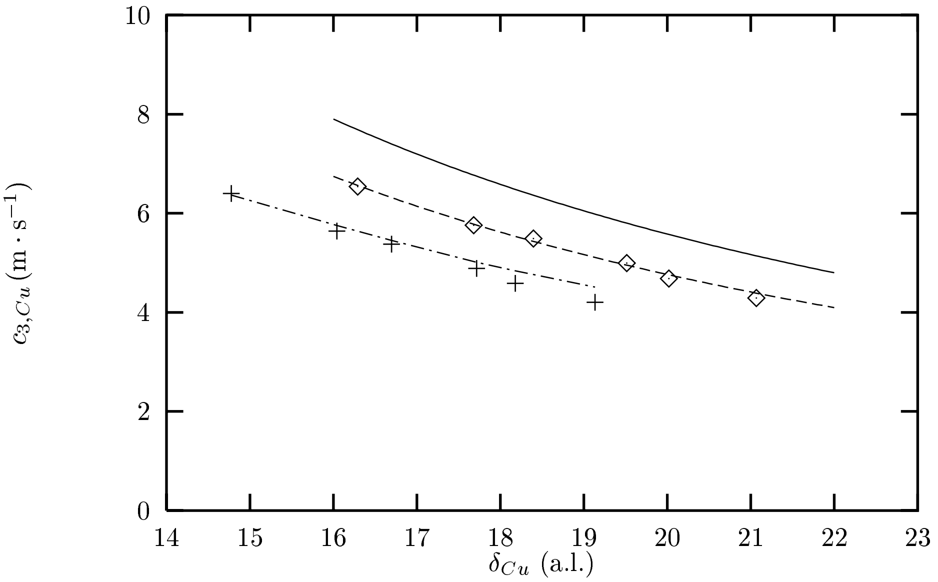

Figure 4.5: Third sound speed $c_{3,Cu}$ on copper as a function of ^{4}He film thickness δ_{Cu}. $\diamond$ and solid line: Experimental results and theoretical relation, respectively, using $\gamma_{Cu} = 5.92 \cdot 10^{-24}\,\mathrm{m^5 s^{-2}}$ and $D(T) = 1.91\,$a.l.; Dashes: Theoretical relation with $\gamma_{Cu} = 4.3 \cdot 10^{-24}\,\mathrm{m^5 s^{-2}}$ and $D(T) = 1.91\,$a.l.; + and dots&dashes: Experimental results and theoretical relation, respectively, using $\gamma_{Cu} = 4.3 \cdot 10^{-24}\,\mathrm{m^5 s^{-2}}$ and $D(T) = 5.66\,$a.l.

4.3 Third sound attenuation

4.3.1 Calculation of the attenuation coefficient α

To find the third sound attenuation coefficient α, the amplitudes of the first and second third sound peaks in a third sound signal (like Figure 4.1) are measured. These two peaks represent two third sound waves that were excited, ran some distance without passing the detector or heater, and were detected. They only differ in the distance the waves ran over the substrate surface. A_1 is the amplitude of the first peak, where the third sound wave travelled 1/4 of the bar circumference. A_2 is the amplitude of the second peak. Here the third sound wave travelled 3/4 of the bar circumference. Using the definition of α (Equation 1.6), the ratio of these amplitudes can be used to calculate α:

$$\frac{A_2}{A_1} = \frac{A(0)\, e^{-\alpha(\frac{3}{4}\pi d)}}{A(0)\, e^{-\alpha(\frac{1}{4}\pi d)}} = e^{-\frac{1}{2}\alpha\pi d}$$

Here d is the bar diameter. Now the attenuation coefficient can be calculated if A_2 and A_1 are measured and d is known:

$$\alpha = -\frac{2}{\pi d} \ln \frac{A_2}{A_1}$$

4.3.2 Attenuation on the glass bar

In Figure 4.6 values of the attenuation coefficient α for third sound on the glass bar measured in various experiments are plotted as a function of ^{4}He film thickness δ_{gl} calculated using $c_{3,gl}$ (Equation 1.1). The theoretical values as a function of δ as calculated according to Brouwer[4, 5] in Section 1.3 for $T = 1.21\,\mathrm{K}$ are plotted in the same graph. The data points show a large spread, but agree in order of magnitude with the theoretical predictions.

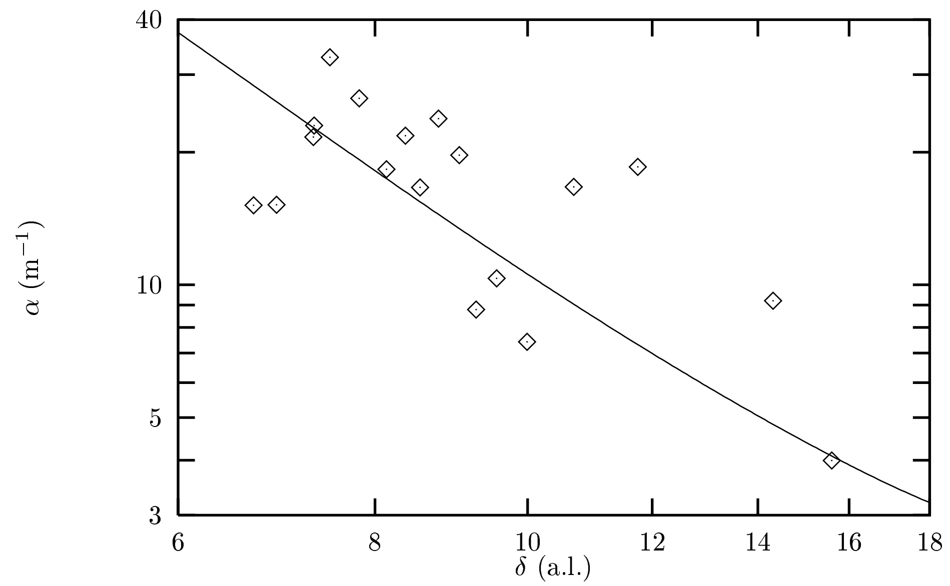

Figure 4.6: Third sound attenuation α on glass as a function of ^{4}He film thickness δ. $\diamond$ Experimental results; Solid line: Theoretical relation according to Brouwer[4, 5]

4.3.3 Attenuation on the copper bar

In Figure 4.7 the attenuation coefficient α for third sound on the copper bar is plotted as a function of ^{4}He film thickness on copper δ_{Cu} calculated using $c_{3,gl}$ according to Section 4.2.2. The theoretical predictions (according to Brouwer, Section 1.3) are also plotted in the same graph. Note the small spread in the data points compared to the results on the glass bar. Also note that the measured attenuation is *lower* than the theoretical value.

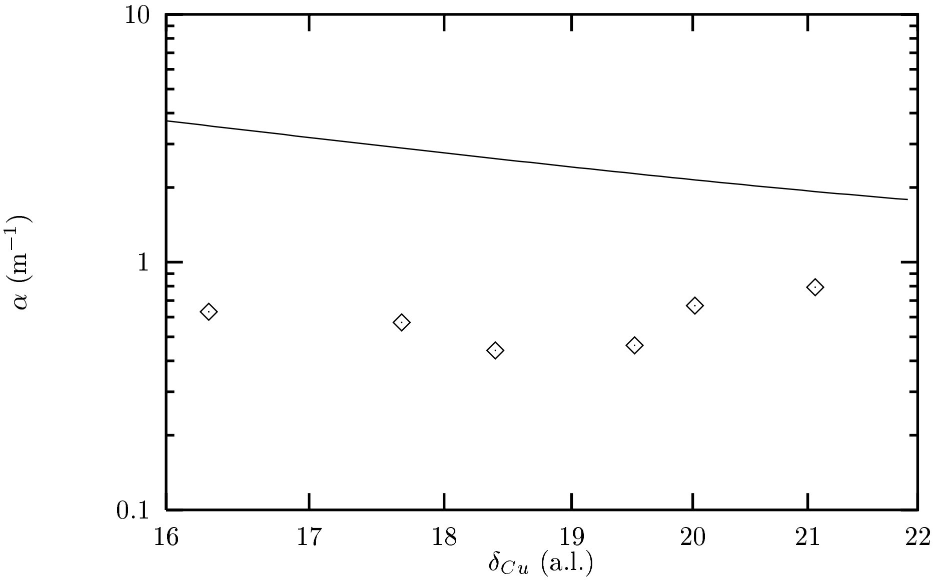

Figure 4.7: Third sound attenuation α on copper as a function of ^{4}He film thickness δ_{Cu}. $\diamond$ Experimental results; Solid line: Theoretical relation according to Brouwer[4, 5]

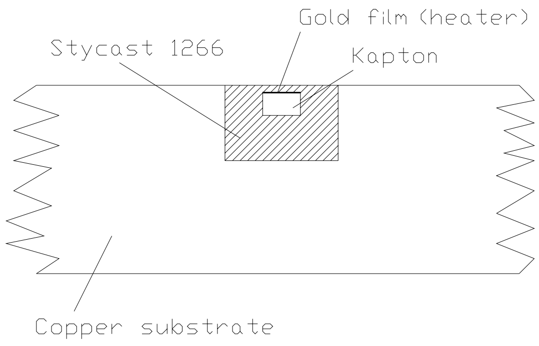

Figure 4.8: Brisson's heater

4.4 Discussion and conclusions

4.4.1 Third sound on copper

In the experiments described here, third sound was seen on a copper substrate, although only on films thicker than ≈ 16 a.l. Pinkse[14] also measured third sound on copper on films thicker than ≈ 12 a.l. only. A possible indication why third sound was not seen on thinner films may be given from the value of the dead layer thickness $D(T)$ needed for the fitting of the theoretical relation for $c_{3,Cu}(\delta_{Cu})$ in Section 4.2. A value of $D(T) = 5.66$ a.l. was found, while the relation for $D(T)$ in Section 1.2 gives a value $D(T) = 1.91$ a.l. for $T = 1.21$ K. This high value of $D(T)$ may explain why third sound could not be seen in thin ^{4}He films. Also, the high thermal conductivity of copper compared to glass may make the excitation of third sound on copper more difficult, because more heat will flow away to the substrate and less heat will be used to excite a third sound wave.

4.4.2 Comparison with Brisson's experiments

Brisson[3] could not see third sound on a copper substrate. An explanation for his failure may be derived from the geometry of Brisson's heater (Figure 4.8), which was different from the geometry of the heater of the Leiden group (Figure 3.7). In Brisson's case heat can flow from the heater (at relatively high temperature) through the bulk Kapton and Stycast into the copper substrate, while the heat flow from the heater to the ^{4}He film is limited by an extra Stycast layer on top of the heater. Such an extra layer is not present in the Leiden setup.

4.4.3 Attenuation coefficient on copper

The attenuation coefficient α on copper measured for various values of film thickness δ_{Cu} amounted to $(0.7 \pm 0.2\,\mathrm{m}^{-1})$ (Figure 4.7). Pinkse[14] also measured the attenuation coefficient on copper and found values of the order of 70 m^{-1}. Pinkse's values are larger than the theoretical values[4, 5], which he attributes mainly to the state of his copper bar: his copper surface is "not polished and rather dirty". The experiments described here, with a polished copper bar, yield an attenuation coefficient lower than the theoretical prediction. Note that a higher value of α could be expected as a result of impurity of the copper surface, but a lower value could not. We have no explanation for this discrepancy. Using the values $\gamma_{Cu} = 4.3 \cdot 10^{-24}\,\mathrm{m}^5\mathrm{s}^{-2}$ and $D(T) = 5.66$ a.l. obtained in Section 4.2 does not bring down the theoretical attenuation coefficient to the measured values. The attenuation coefficient on the glass bar agrees with the theoretical predictions.

4.4.4 Problem: Pressure determination

In the beginning of the experiment, a lead of the pressure gauge outside the cryostat broke because someone tripped over the wire. Repairing it shifted the capacitance by an unknown amount, making pressure determination impossible. For proper calibration, the capacitance at zero pressure and low temperature is needed. This value could not be determined as it was not possible to pump all the helium out of the cell without warming up. When cycling from 4.2 K to higher temperature and back there is a capacitance shift.

New cables were used for the leads of the pressure gauge, because the old cables caused capacitance shifts as a result of (unavoidable) vibrations. For both leads now a coaxial cable was used. Also a different, more stable capacitance bridge was used to determine the capacitance of the pressure gauge. The new bridge could measure capacitances of 50 pF with a sensitivity of 0.0001 pF, corresponding with a pressure of 0.007 mbar. The new bridge has not been used for the experiments described in this chapter.

4.4.5 Problem: Film thickness determination error

For the thickest films, the film thickness δ was calculated both from the amount of ^{4}He admitted to the cell, n_{in}, and from the third sound speed on glass, $c_{3,gl}$. The film thickness could not be determined from the vapour pressure in the cell because of the problems with the pressure gauge described above. The first method used Equation 1.16. Using the values of n_{in} and $c_{3,gl}$ for the thinnest film measured, $n_{\text{in}} = 6.20\,\text{mmol}$ gives a film thickness $\delta = 35.1\,\text{a.l.}$ while $c_{3,gl} = (23.4 \pm 0.9)\,\text{m}\,\text{s}^{-1}$ gives $\delta = 5.6\,\text{a.l.}$ For the thickest film measured, $n_{\text{in}} = 35.9\,\text{mmol}$ gives $\delta = 250$ a.l. while $c_{3,gl} = (5.02 \pm 0.22)\,\text{m}\,\text{s}^{-1}$ gives $\delta = 16.4\,\text{a.l.}$ Note that deteriotation of the copper sinter or capillary condensation of ^{4}He in the sinter can not be held responsible for the high values of δ calculated from n_{in}, because a smaller sinter surface would give an even higher film thickness (the same amount of ^{4}He would spread out over a smaller surface).

A possible explanation for the discrepancy in the value for the ^{4}He film thickness calculated from the amount of ^{4}He admitted to the cell and from the third sound speed on glass may be that most of the helium that was let into the cryostat may end up in the filling capillary in stead of in the cell, because of counterflow effects in the capillary. The inside of the filling capillary is covered by a superfluid helium film from the cell up to the helium level in the bath. Above the helium level the capillary gets warmer, reaching room temperature at the top flange. Around the superfluid transition (2.17 K) the helium film will get very thick, while the vapour pressure reaches 50 mbar. A superflow up in the film combined by a flow of gas down may trap a lot of helium. To be able to work around this problem, a low-temperature valve was fitted just above the cell. Using this valve the filling capillary can now be closed. By admitting helium to the cell at temperatures larger than 2.17 K and closing the valve during cooldown it was hoped to solve the problem. New experiments may show if this extra valve indeed solves the problem.

Appendix A

Drawings

This appendix contains the drawings A.1 to A.6 that were made, mostly for the parts of the cell.

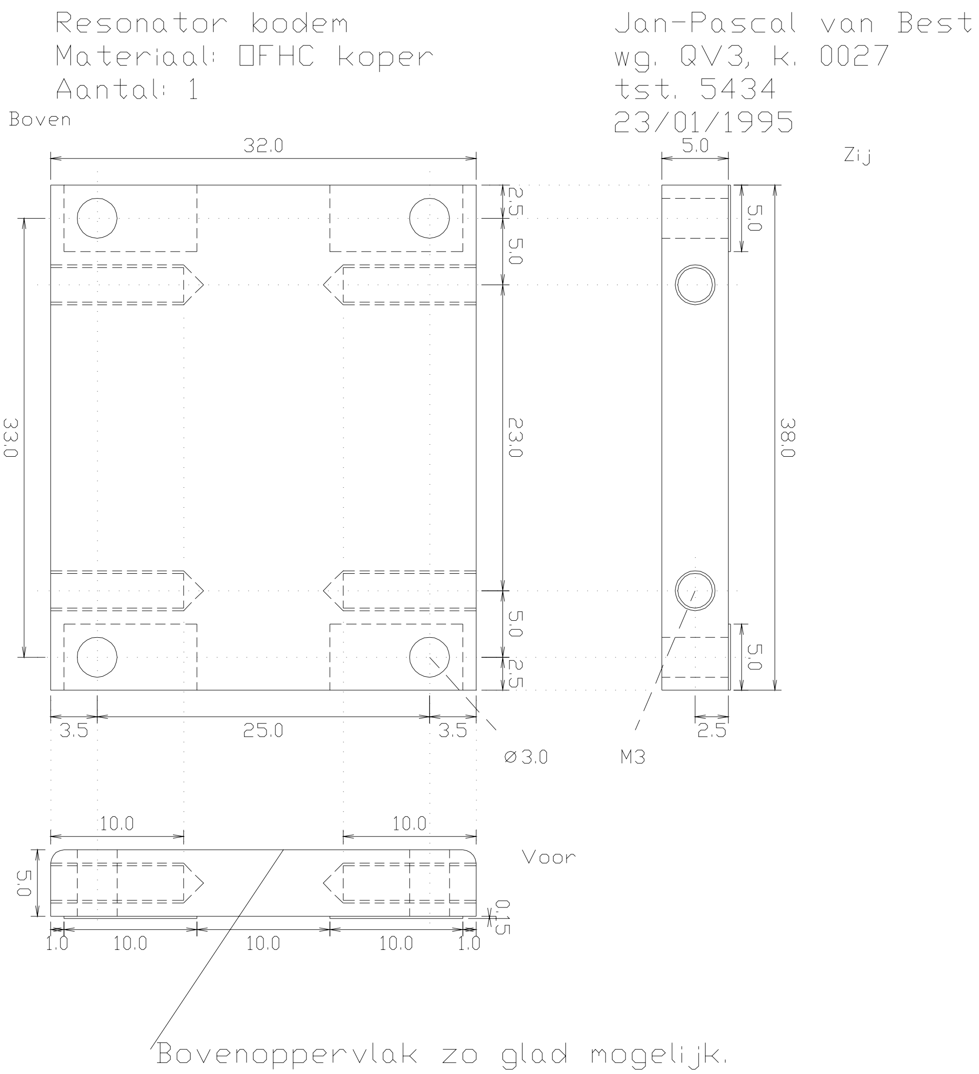

Figure A.1: Bottom plate in experimental cell

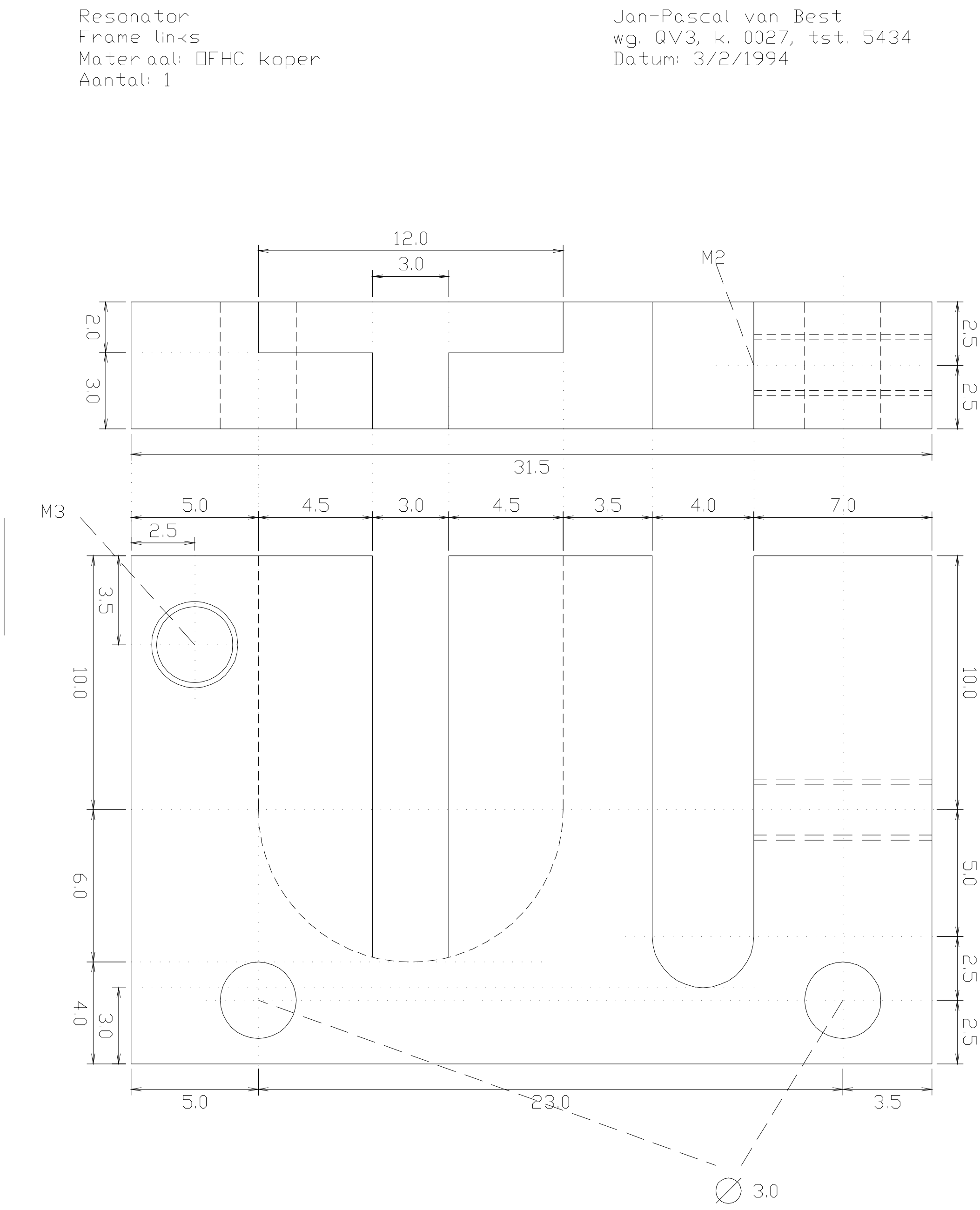

Figure A.2: Left frame piece

Resonator
Frame Rechts
Materiaal: OFHC koper
Aantal: 1

Jan-Pascal van Best
wg. QV3, k. 0027, tst. 5434
Datum: 3/2/1994

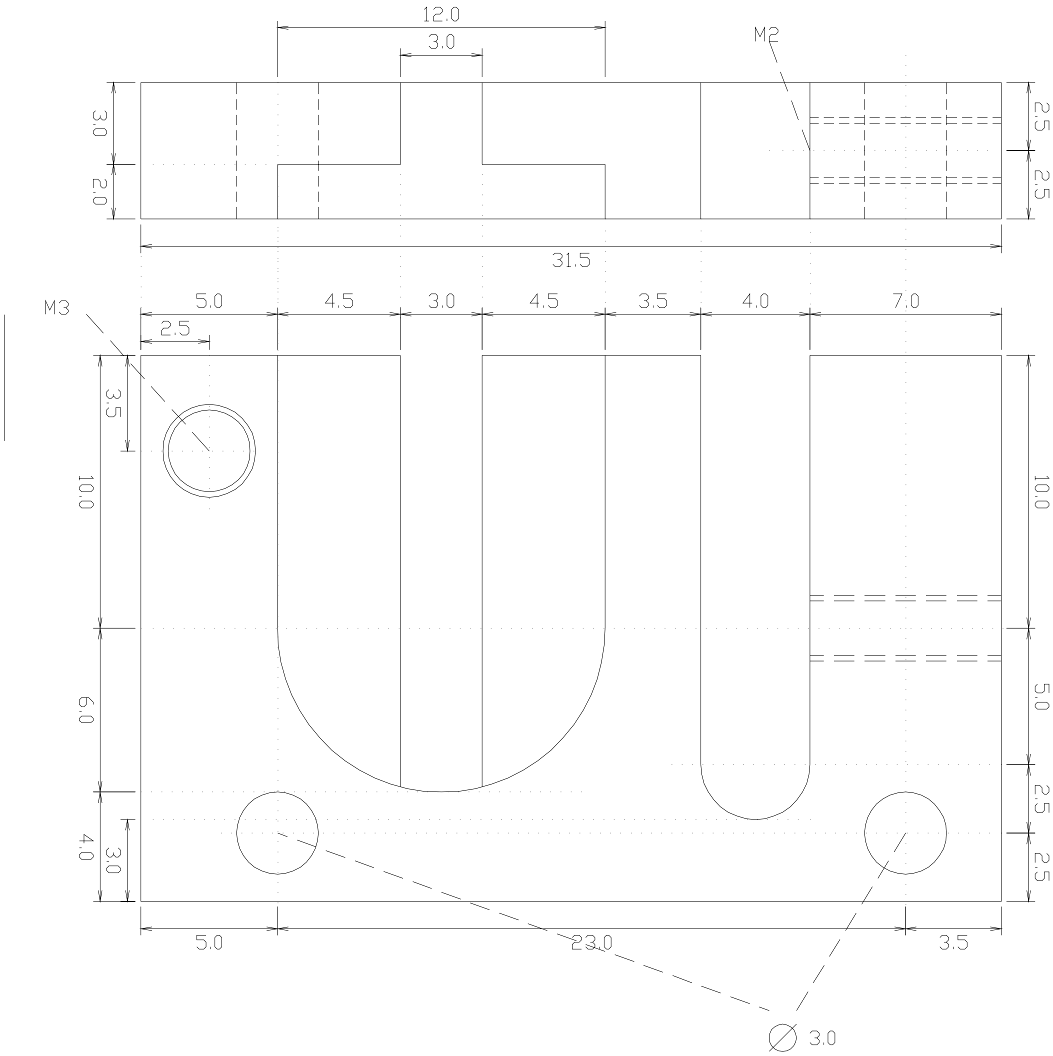

Figure A.3: Right frame piece

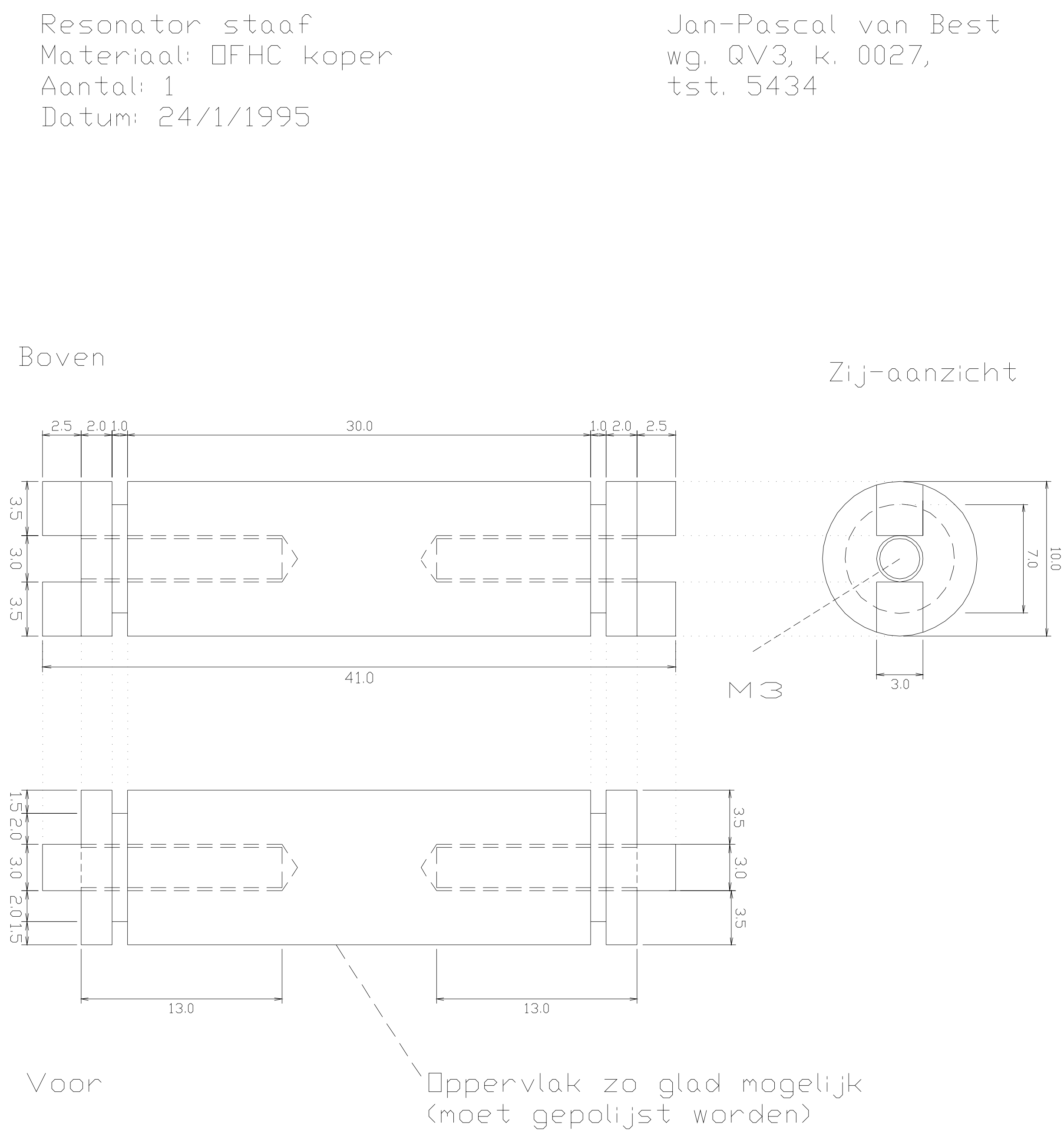

Figure A.4: Copper resonator bar

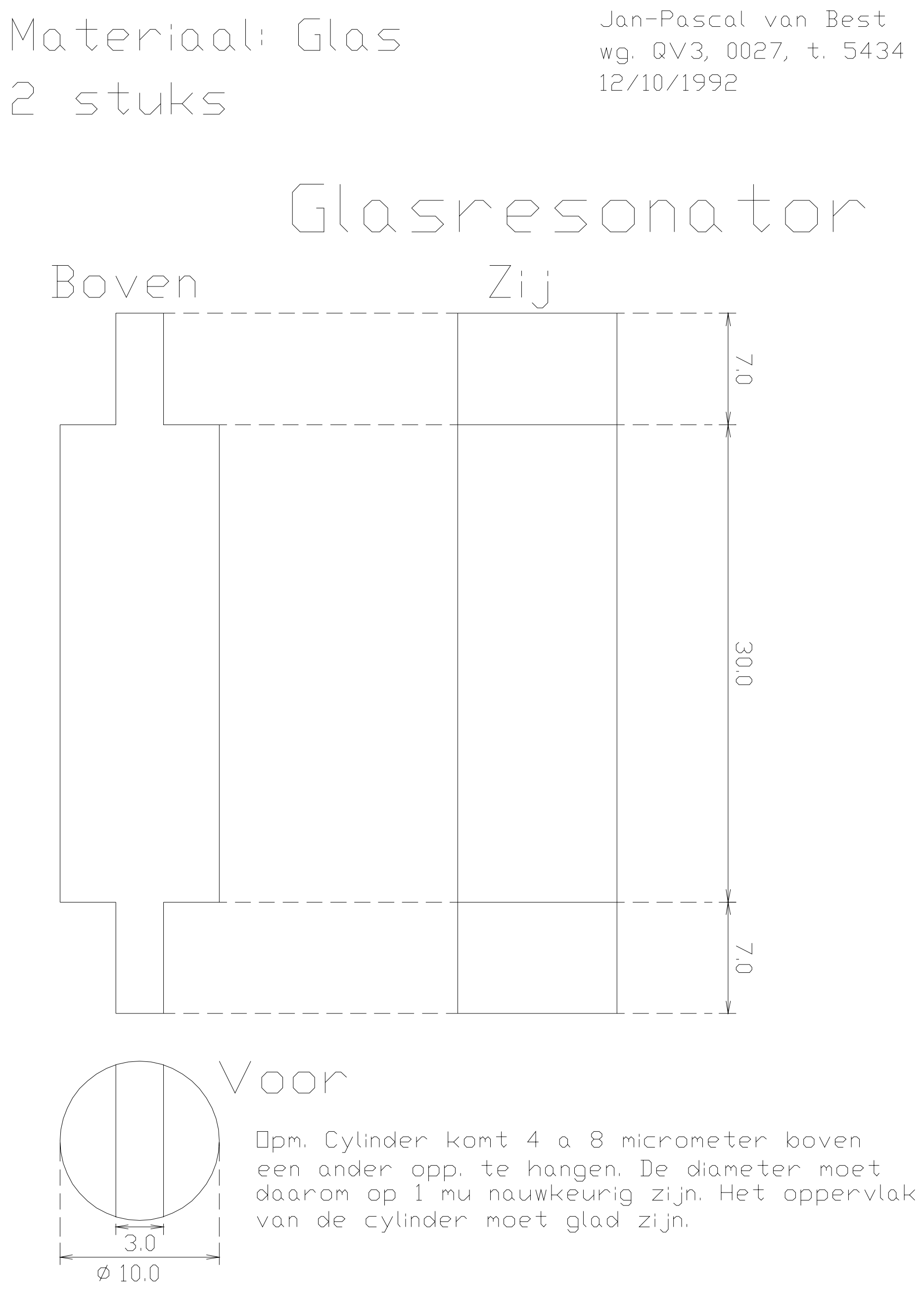

Figure A.5: Glass resonator bar

Mounting Platform
Material: OFHC copper
Number: 1

Jan-Pascal van Best
wg. QV3, k. 0027, tst. 5434
Date: 26/1/1994

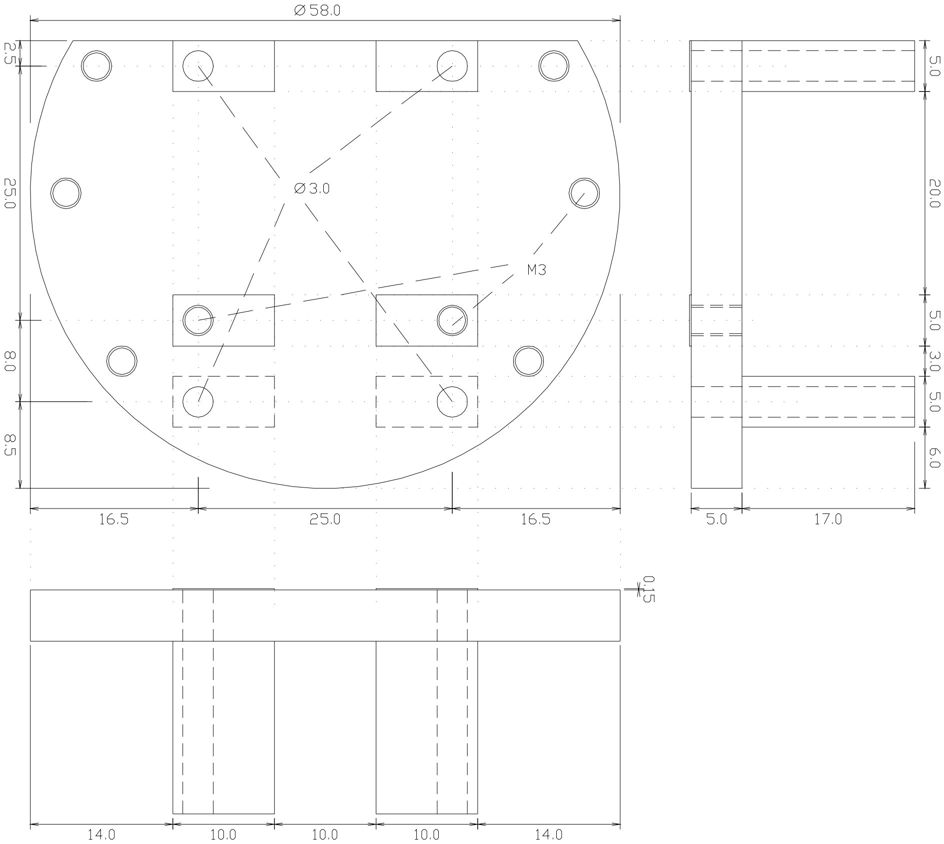

Figure A.6: Mounting platform

Appendix B

Symbols

Symbol	Unit	
A	m^2	Area for heat flux ($A = L_x \cdot L_y$)
$A(x)$	m	Third sound amplitude as a function of distance
$a.l.$	m	Atomic layer or 0.36 nm
c	$\mathrm{m\,s^{-1}}$	Sound speed
$c_{3,gl}$	$\mathrm{m\,s^{-1}}$	Third sound speed on glass
$c_{3,Cu}$	$\mathrm{m\,s^{-1}}$	Third sound speed on copper
d	m	Bar diameter
$D(T)$	m	Dead layer thickness
E	J	Energy
$f_{BE}(x)$		Bose–Einstein distribution function, $f_{BE}(x) = \frac{1}{e^x - 1}$
$f(\delta)$	$\mathrm{m\,s^{-2}}$	Van der Waals attractive force
$g(\omega)$	s	Density of states over ω
$g(\vec{k})$	m^3	Density of states over $\vec{k}$
$g_\Omega(\theta)$		Density of states (with $\omega < \Omega$) over θ
$\hbar$	Js	Dirac's constant
$\vec{k} = (k_x, k_y, k_z)$	m^{-1}	Wave vector
k_B	JK^{-1}	Boltzmann's constant
L_x, L_y, L_z	m	Crystal dimensions
m	kg	mass of a ^{4}He atom
$N = N_x \cdot N_y \cdot N_z$		Number of atoms in the crystal
$N_{\omega_{\vec{k}}<\omega}$		Number of $\vec{k}$-values with $\omega_{\vec{k}} < \omega$
N_{film}		Number of atoms in the ^{4}He film
N_{vapour}		Number of atoms in the ^{4}He vapour
N_0		Number of "extra" ^{4}He atoms in the first one or two layers
n	m^{-3}	^{4}He number density; $n = (1\,\mathrm{a.l.})^{-3}$
n_{in}	mol	Number of ^{4}He atoms in the cell

Symbol	Unit	
p_v	Pa	Vapour pressure
p_{sv}	Pa	Saturated vapour pressure
$\dot{Q}$	W	Heat flux through a surface
R	$\mathrm{Jmol^{-1}K^{-1}}$	Ideal gas constant, $R = 8.31411\,\mathrm{Jmol^{-1}K^{-1}}$
R	$\mathrm{KW^{-1}}$	Thermal resistance
R_K	$\mathrm{K^4m^2W^{-1}}$	Kapitza resistivity
S	$\mathrm{m^2}$	Surface area
T	K	Temperature
V	$\mathrm{m^3}$	Volume ($V = L_x \cdot L_y \cdot L_z$)
V_{tot}	$\mathrm{m^3}$	Room temperature volume for ^{4}He admission
$\mathcal{Z}$		Set of integer numbers
$\alpha(\theta)$		fraction of phonons, coming in at an angle θ, that cross the interface
α	$\mathrm{m^{-1}}$	Attenuation coefficient
β	a.l.	Retardation constant ($\beta = 15$ nm for glass)
γ	$\mathrm{m^5s^{-2}}$	Van der Waals constant
γ_{gl}	$\mathrm{m^5s^{-2}}$	Van der Waals constant for glass ($\gamma_{gl} = 2.6 \cdot 10^{-24}\,\mathrm{m^5s^{-2}}$)
γ_{Cu}	$\mathrm{m^5s^{-2}}$	Van der Waals constant for copper
$\delta(x)$		Dirac delta function
δ	m	^{4}He film thickness
δ_{gl}	m	^{4}He film thickness on glass
δ_{Cu}	m	^{4}He film thickness on copper
θ, ϕ		Angular coordinates of wave vector
λ	m	Wavelength
$\left(\frac{\rho_s}{\rho}\right)$		Superfluid fraction in bulk ^{4}He
$\left(\frac{\rho_s}{\rho}\right)_f$		Superfluid fraction in a ^{4}He film
ω	$\mathrm{s^{-1}}$	Circular frequency
Ω	$\mathrm{m^2s^{-2}}$	Van der Waals potential
Ω_{gl}	$\mathrm{m^2s^{-2}}$	Van der Waals potential on glass
Ω_{Cu}	$\mathrm{m^2s^{-2}}$	Van der Waals potential on copper
$\omega_{\vec{k}}$	$\mathrm{s^{-1}}$	Circular frequency corresponding with wave vector $\vec{k}$ ($\omega_{\vec{k}} = c\left\|\vec{k}\right\|$)
$\lfloor x \rfloor$	$[x]$	Largest integer smaller than or equal to x

Bibliography

[1] H. van Beelen, *syllabus "Twee-fluïda Hydrodynamica"*, Leiden University, 1994

[2] J.P. van Best, Pascal software for Monte Carlo experiments on phonon densities, `http://qv3pluto.leidenuniv.nl/jvbest/phonon/`, Leiden University, 1996.

[3] J.G. Brisson II, *Third Sound Studies of Helium on Molecular Hydrogen*, Harvard University, Cambridge MA, U.S.A, 1990

[4] P.W. Brouwer, *Derde Geluid – Theorie*, B.Sc. Thesis, Leiden University, 1992

[5] P.W. Brouwer, Pascal software for calculating third sound properties, `http://qv3pluto.leidenuniv.nl/jvbest/thirdsound/`, Leiden University, 1992.

[6] J. Richard Christman, *Fundamentals of Solid State Physics*, Wiley, New York, 1988. p. 216

[7] W.A. Draisma, *Third sound in pure ^{4}He and ^{3}He-^{4}He mixture films*, Ph.D. Thesis, Leiden University, 1993

[8] M.E.W. Eggenkamp, *On 2D Heat Diffusion through a Glass Substrate Coated by Helium*, M.Sc. Thesis, Leiden University, 1992

[9] M.E.W. Eggenkamp, H. Khalil, J.P. Laheurte, J.C. Noiray, and J.P. Romagnan, Heat diffusion through a glass substrate coated by a thin ^{4}He film, in *Europhys. Lett. 21* (1993), 587-592

[10] W.E. Frick, D. Waldmann, and W. Eisenmenger, Phonon Emission Spectra of Thin Metallic Films, in *Appl. Phys. 8* (1975), 163-171

[11] I.M. Khalatnikov, *An Introduction to the Theory of Superfluidity*, 1965

[12] W.A. Little, The Transport of Heat between Dissimilar Solids at Low Temperatures, in *Can. J. Phys. 37* (1959), 334-349

[13] J.C. Mester, E.S. Meyer, M.W. Reynolds, T.E. Huber, and I.F. Silvera, Heat Transport via Evaporation of Superfluid Helium Films: Giant Effective Kapitza Resistance, in *Phys. Rev. Lett. 68* (1992), 3068-3071

[14] P. Pinkse, *New techniques in a third sound study*, M.Sc. Thesis, Leiden University, 1992

[15] P. Remeijer, *Thermal and electromechanical excitation of third sound in Helium films*, M.Sc. Thesis, Leiden University, 1990

[16] P. Shirron, K. Gillis, J. Mochel, in *J. Low Temp. Phys. 15* (1989), p. 349

[17] W.J.McG. Tegart, *The Electrolytic and Chemical Polishing of Metals*, London, Pergamon Press, 1959

[18] J. Wilks and D.S. Betts, *And Introduction to Liquid Helium*, Oxford Science Publications, Oxford